Shock Compaction of Graphene Doped Yttria Stabilized Zirconia: An Experimental and Computational Study

Christopher Rueben Johnson
Marquette University

SHOCK COMPACTION OF GRAPHENE DOPED YTTRIA STABILIZED ZIRCONIA: AN EXPERIMENTAL AND COMPUTATIONAL STUDY

by

Christopher Johnson

A Thesis submitted to the Faculty of the Graduate School,
Marquette University,
in Partial Fulfillment of the Requirements for
the Degree of Master of Science

Milwaukee, Wisconsin

May 2019

ABSTRACT
SHOCK COMPACTION OF GRAPHENE DOPED YTTRIA STABILIZED ZIRCONIA: AN EXPERIMENTAL AND COMPUTATIONAL STUDY

Christopher Johnson

Marquette University, 2019

Yttria stabilized zirconia (YSZ) is a broadly used ceramic due to its impeccable hardness and thermal stability. Limitations of the material, however, subsist within its fracture toughness. Literature indicates that shock consolidation may enable production of composite YSZ and graphene mixtures with improved fracture toughness and other material properties while maintaining the material's nanostructure dimensionality. Therefore, investigation of the compaction phenomena at non-equilibrium states will provide informative results to be used for the fabrication of bulk graphene-YSZ composites.

Computational molecular dynamics (MD) simulations and impact experiments are conducted to explore and characterize the dynamic response of the YSZ variants. Molecular dynamics simulations studied bulk Hugoniot response observed for various graphene and YSZ mixtures. Impact experiments compacted YSZ and graphene/YSZ variants at velocities spanning 300-600 m/s. Two distinct particle sizes of YSZ were investigated (micrometer and nanometer), as well as weight percentage of graphene added to the YSZ (0%, 1%, 3%, 5%). Experimental results portray many physical mechanisms exhibited during the compaction/consolidation process, such as heterogeneity and porosity. Comparison of the MD and experimental results map the thermodynamic state of the materials, defining the non-equilibrium states exhibited by the specimens.

ACKNOWLEDGMENTS

Christopher Johnson

Completion of this work could not have been accomplished without the generosity and care of many people, to whom I would like to express deep appreciation and gratitude towards:

To my advisor Dr. John Borg, for the opportunity to pursue further education, and the ability to grow as a person, scientist, and professional. He has given myself and many students countless opportunities, for which we are all incredibly thankful.

To my close friends of the Marquette Shock Physics Lab, thank you Jeff, Peter, and Nathaniel for the many conversations, laughs, and memories.

To the Marquette faculty and staff, thank you for challenging and pushing individuals such as myself to think deeply and critically in an academic setting.

To Mr. David Newman, Mr. Thomas Silman, Mr. Robert (Geno) Johnson, and Mr. Randal Dusel, thank you for your continuous lessons and guidance over the past two years.

To my family, friends, and girlfriend, thank you for the endless support, love, and direction.

To the Air Force Office of Scientific Research and Oceanit for the grant which supported this research. This opportunity would not have been possible without your support.

TABLE OF CONTENTS

LIST OF TABLES

LIST OF FIGURES

CHAPTER

1 INTRODUCTION

1.1 Motivation

Shock consolidation of powders fosters a promising technique for the fabrication of bulk materials with tailorable mechanical, thermal and electrical behavior. The Air Force Office of Scientific Research (AFOSR) is interested in studying such phenomena, aiming to characterize the dynamic response, material properties, and phase of ceramic variants. With this characterization, greater understanding of material behavior under non-equilibrium conditions will allow informative decisions to be made regarding heterogeneous structures and consolidation techniques used during manufacturing processes. In collaboration with Oceanit, this work seeks to study an array of ceramic materials using computational molecular dynamics (MD) and impact experiments performed with a light gas-gun. Such approaches characterize the non-equilibrium thermo-mechanical states of graphene and yttria stabilized zirconia (YSZ) compositions.

Yttria stabilized zirconia (ZrO_2-Y_2O_3) is a technologically important material used in many metallurgic applications [1]. Oxide fuel cells [2], [3], oxygen sensors [4], and ceramic membranes [5] are several specific applications. Although YSZ is broadly used, its ability to elevate fracture strength, as well thermal and electrical conductivity, could serve a wider array of military, ecological, and industrial applications.

Carbon nanomaterials, such as graphene and carbon nanotubes (CNT), have been investigated as reinforcement additives in polymers, metals, and ceramics [6] [7]. Literature indicates the addition of graphene to YSZ may increase rigidity of the bulk

composite, decreasing the brittle nature and increasing the fracture toughness of the ceramic body [8]. Such approach is analogous to the addition of rebar to concrete for increased mechanical strength. Similar results would broaden use in many additional applications.

Currently, minute computational and experimental work has been conducted to analyze the shock response of graphene and YSZ mixtures. Computational studies found in literature indicate numerous individual have studied the molecular dynamics of YSZ [1], [9]–[11] and graphene [12]–[14], however, no works were found to have studied mixtures of the two species. In 1990, experimental work performed by Mashimo [15] analyzed the shock response of cubic YSZ using impact experiments performed with a gun system. Additionally, in 2015 Sable [16] analyzed the dynamic compaction of YSZ with carbon nanotubes (CNT) and YSZ mixtures. Therefore, this experimental and computational characterization of the shock compaction of graphene-YSZ mixtures seeks to provide further insight on the dynamic behavior at the atomic and continuum scales.

1.2 Literature Review

The culmination of shock physics research has led to an increased understanding of the dynamic behavior of the compaction of materials. Although literature covers a wide array of topics associated with shock compaction, reoccurring themes emerge which highlight the mechanics and implications of shock consolidation. They are consolidation techniques, material compositions, implications of grain size and porosity, and the affinity to enhanced material properties. This review focuses on detailing these themes, setting the necessary foundation for the conducted research.

Prior to discussing the implications of shock consolidation, it is quintessential to understand the experimental techniques which can be used to consolidate a material using shock waves. Three prominent techniques appear in the literature: explosively driven devices [17]–[19], laser shock sintering [4] [5], and gun systems [16], [22]–[25]. Each method possesses unique capabilities, ideal for specific applications.

Explosively driven devices induce a shock front using an energetic mechanism, where experimental design is typically of cylindrical shape, with an explosive charge oriented on the top face of a cylinder and a sample located within the cylinder [17]–[19]. The region between the sample and cylinder can be filled with a variety of different mediums (water, steel, etc.), aiming to cater to a specimen's dynamic response. When detonated, the explosive imparts an extreme amount of pressure which propagates through the surrounding components, densifying (compacting) traversed materials. Ultimately, explosively driven devices are a cost-effective mechanism for consolidation experiments, however, safety concerns arise due to the use of energetic materials and are limited to the highest regime of loading conditions. Additionally, the ability to recover a specimen post-experiment is difficult.

Laser shock sintering functions by exerting a mechanical force onto a sample using a high intensity laser. In experiments, a material of interest is placed in a substrate with a highly absorptive paint applied to the exposed sample surface. A thin layer of transparent dielectric material (typically glass) is then overlaid on the painted surface. To agitate a shockwave, an incident laser pulse is transmitted through the dielectric surface creating plasma from the highly absorptive paint [21]. The resulting thermodynamic effects densify the specimen, causing compaction of the powdered specimen. Such

technique presents a unique consolidation mechanism with quick turnaround, however, concerns arise over the uniformity of the shock front imposed on the sample.

The final technique, achieved using a gun system, accelerates a projectile to a given velocity (100-30,000 m/s [26]), impacting a target containing the sample of interest. Projectiles can be driven using electro-magnetic waves (rail gun), explosives (propellant/powder gun), or gaseous substances (light gas-gun). There are various assemblies for each gun type which produce a range of projectile velocities. Gas guns will be emphasized here, and are traditionally used for lower echelon velocities (<1500 m/s), while propellant guns are used for medium velocities (1500 m/s – 8000 m/s), and rail guns are used for high velocities (8000 m/s – 15,000 m/s). Notoriety for gun systems can be attributed to the inherent experimental consistency, control, and the ability to recover specimens post-experiment.

Previously described experimental techniques have been utilized in numerous studies analyzing the compaction and consolidation of powders. Early studies date back to the 1980's where studies conducted by Kasiraj, Schwarz, Ahrens, and Akashi investigated alloy steel (AISI 9310) powder [23], [27], aluminum lithium powders [28], and silica carbide [29]. The 1990's yielded work from Tong [25] and Hokamoto [17] analyzing materials such as Ti-SiC, TiB_2 and c-BN. The dawn of the twenty first century yielded work from Marquis [30] and Sh [31] investigating tungsten based heavy alloys and alumina based nanoparticles. The present decade has seen work from numerous scientists, such as; Fredenburg [24], [32], Ahn [22], Zhou [18], Beck [19], and Deng [21] whom explored the densification of an array of ceramics, metallic, and other composite materials.

With this vast collection of materials studied, heterogeneity, grain structure, grain interaction, and porosity have been determined to play a fundamental role in the consolidation of materials. Theory of the stated mechanisms have been investigated by Borg [33], Meyers [34], Lane [35], and Fenton [36] through computational studies and mesoscale modeling techniques. Prior to these, many works aimed to model material dynamics at the continuum scale, neglecting mesoscale effects such as grain structure, grain to grain interaction, and porosity. Phenomena of such dictate many material characteristics exhibited in the consolidated material, as discussed in many of these works. Greater attention towards understanding these mesoscopic characteristics have generated greater understanding for the theory of densification, and increased affinity for the formulation of new composites using micro-powders and nano-powders which may produce metastable materials.

1.3 Objectives and Methodology

Objectives of this work aim to study and characterize the dynamic behavior of graphene and YSZ mixtures. Computational and experimental studies proceed in the following. Molecular dynamics simulations will leverage near perfect crystalline structures to investigate the shock response and thermodynamic state of graphene and YSZ mixtures. Representative ensembles of atoms will be compressed, emulating the idealized shock responses (Hugoniot responses) of a bulk material on a molecular scale. Experimental work will aim to characterize the shock response of eight varied compositions of porous, heterogeneous, graphene and YSZ mixtures. Studies will be

performed over a variety of pressure states, and focus on two variables: YSZ particle size and graphene weight percentage.

Computational and experimental studies provide insight into the atomic, mesoscopic, and continuum scale response of the materials. Comparison of length scales will illustrate implications of the porosity and heterogeneity observed in the impact experiments. It is hypothesized that results of the MD simulations may result in significantly different Hugoniot response (larger shock velocities and density states) than experimental data, indicative of the porosity and heterogeneity of the powdered experimental samples. This statement is formed from comparison between Mashimo and Sable's experimental data. It is also believed that the shock response of the YSZ particle sizes (nanometer and micrometer) and graphene weight percentage (0%,1%,3%,5%) will yield higher shock velocities as the graphene weight percentages are increased. A statement of such is based off the results of Sable's data. These results are highly dependent on the initial density of the samples, and will be likely easier to achieve with smaller grain sizes. Higher packed densities will reduce the porosity of the sample, and potentially result in higher shock velocities.

2 INTRODUCTION TO SHOCK PHYSICS AND THE MECHANISMS OF SHOCK CONSOLIDATION

The following subsections outline the rudimentary equations and foundational mechanisms defining the shock response of a material. These relations will be used to compare the results of MD simulations with the experimental data. First, a brief introduction to shock physics is addressed, and is followed by an introduction to the Rankine-Hugoniot jump equations. Discussion of equation of state (EOS) modeling in relation to the Rankine-Hugoniot jump equations then proceeds. Finally, the mechanisms of shock consolidation are conveyed, forming an understanding of the implications of rapid compression of granular heterogeneous medias.

2.1 Shock Wave Background

Physically, a shock wave is a propagating disturbance that moves faster than the local sound speed of a material. This disturbance is induced by an energy front traversing through a medium. Such phenomenon causes a plethora of physical effects due to the compressibility of the medium, and are dependent on the properties of the material. The physical nature of a shockwave results in nearly discontinuous property changes at the continuum scale, where affected regions of the shock can result in enhanced densification [37]. Because of the inherent thermodynamic nature of rapidly compressing a material, the continuity equation, momentum equation, energy equation, and equations of state can be coupled to quantitatively describe the phenomenon.

2.2 Rankine-Hugoniot Jump Equations

The fundamental equations which mathematically describe a shock wave are known as the Rankine-Hugoniot jump conditions, and institute the conservation of mass, momentum, and energy of any shocked system (Equations 2.1 - 2.3). Five parameters comprise the equations: shock velocity (U), particle velocity (u), pressure (P), density (ρ), and specific internal energy (e) [38]. Such parameters detail material properties on both sides of a shock front. An illustration of the discontinuity can be visualized in Figure 2.1, where subscripts 0 and 1 denote the states directly ahead and behind the shock front.

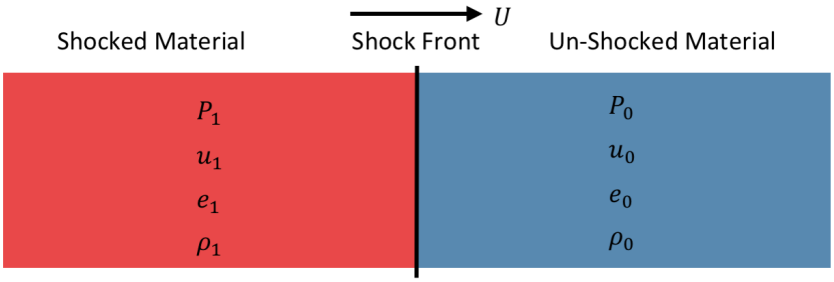

Figure 2.1: Illustration of the shock parameters in shocked and un-shocked materials.

Mass:
$$\frac{\rho_1}{\rho_0} = \frac{U - u_0}{U - u_1} \tag{2.1}$$

Momentum:
$$P_1 - P_0 = \rho_0(u_1 - u_0)(U - u_0) \tag{2.2}$$

Energy:
$$e_1 - e_0 = \frac{P_1 u_1 - P_0 u_0}{\rho_0(U - u_0)} - \frac{1}{2}(u_1^2 - u_0^2) \tag{2.3}$$

There are two characteristic velocities in a shock propagation: shock and particle velocity. A fundamental relationship exists between the two velocities, and can be conceptualized through a simple example. Imagine shoveling snow, where one pushes a shovel into a fresh untouched region. As the shovel starts to accumulate snow, a ripple can be noticed at a given distance away from the shovel. This "front" in the snow is analogous to a shock front, and travels at what is referenced as the shock velocity (U). Additionally, one can observe that there is also a velocity associated with the shovel pushing the snow behind the ripple. This is referenced as the particle velocity (u) of a shocked system. With these two velocities defined, an important relationship emerges which can be utilized to formulate equations of state for a given materials by solving equations 2.1 - 2.3 for various parameters.

Mass ($u_0 = 0$):
$$\frac{\rho_1}{\rho_0} = \frac{U}{U - u_1} \tag{2.4}$$

Momentum ($u_0 = 0$):
$$P_1 - P_0 = \rho_0 u_1 U \tag{2.5}$$

Energy ($u_0 = 0$):
$$e_1 - e_0 = \frac{P_1 u_1}{\rho_0 U} - \frac{1}{2} u_1^2 \tag{2.6}$$

Equations 2.1 - 2.3 present the mass, momentum, and energy equations in terms of the shock system presented in Figure 2.1. Assumptions can be used to simplify these equations, reducing the variable count. A common scenario is for the un-shocked material to be at rest ($u_0 = 0$), where simplifications can be found in equations 2.4 - 2.6. It can be noticed in equations 2.4 - 2.6 that there are five variables (P, U, u, ρ, e) and three

equations (mass, momentum, energy). Therefore, additional equations are needed to close the system and solve the set of equations. Thermodynamic relations known as equations of state are traditionally utilized to close the mathematical system.

2.3 Equations of State

An equation of state (EOS) can be defined as any equation which relates pressure, temperature, and specific volume to describe the state of matter under a given physical condition [39]. Each equation depicts the locust of states in which a material can exist under shock loading, and can be combined to eliminate the energy variable, e, from the energy equation in the conservation set [38]. Relations are typically determined through an experimental series, and can be combined in various thermo-mechanical planes, such as: $U-u,\ U-\rho,\ P-u,\ P-\rho\ ,$ and $P-U$. Common Hugoniot planes determined from experimental sets are $U-u$, $P-\rho$, and $P-u$, and prove to be powerful relations for understanding and identifying the dynamic response and phase changes of a given material. For heterogeneous and porous media, pressure-strain space $(P-\epsilon)$ is a valuable plane which can be used for observations to be made regarding the compressibility of materials in a non-dimensional space.

Hugoniot planes are useful for identifying crystalline changes and final density state of a sample. As previously mentioned, the $U-u$ relation depicts the locus of shock velocities and particle velocities attained through experimental testing. The relationship is linear in nature, however, change in slope may indicate phase change or a shift in the crystal lattice of the material [38]. Equation 2.7 is representative of the $U-u$ relationship, where U, C_o, s, and u are the shock velocity, un-shocked sound speed of the

material (rough approximation), rate of change between the relations, and particle velocity, respectively. Pressure-density space, although not as indicative of phase change, is also a valuable relation that can be used to calculate a wide array of parameters. This relation can be used to calculate the shock velocity if the initial and final density states are known, as well as calculate the final $P-\rho$ state if the initial density state and shock velocity are known [38]. Such relation is important in understanding the ramification of porosity within a sample, and will be used to study strain exhibited by the materials (Equation 2.8, where v_0 and v_1 $(1/\rho_0$ and $1/\rho_1)$ denote specific volume).

$$\mathrm{U} = C_o + su \tag{2.7}$$

$$P = \frac{C_o^2(v_0 - v_1)}{\left(v_0 - S(v_0 - v_1)\right)^2} \tag{2.8}$$

2.4 Mechanisms of Consolidation

Shock consolidation utilizes energy from a shock wave to densify a powdered material via plastic deformation, capitalizing on eight physical mechanisms. They are: microkinetic energy, void collapse energy, melting energy at particle surfaces, defect energy, reaction bonding energy, fracture energy, and friction energy [34]. As a shock wave passes through a sample, high pressures (GPa) are rapidly imposed for several microseconds causing nearly discontinuous thermodynamic responses. The imposed pressure collapses and compresses voids and particles, where particle interactions spur friction and local heating on interfaces. This rapid compression densifies a sample, and

potentially bonds particle interfaces. Resulting particle to particle bonds make this technique a viable option for fabricating bulk materials while maintaining the nanostructure dimensionality of the materials. Caveats, however, exist for inducing such immense and rapid pressures on a specimen. Internal defects attributed to the powdered sample such as vacancies, dislocations, and twinning may also result in undesired features. The stated mechanics of consolidation are considered in the following experiments.

3 MOLECULAR DYNAMICS SIMULATIONS

Computational tools may provide a mechanism to emulate real world phenomena through physically accurate modeling. Advantages can be attributed to the inexpensive ability to explore and emulate physics without performing costly and labor intensive experiments. Two modeling tools will be used in this work to connect the computational and experimental regimes: LAMMPS and CTH. LAMMPS will be used to study molecular response of graphene and YSZ mixtures, while CTH will be used for experimental design discussed in Section 4. The following section introduces MD simulations, implications to this work, and preliminary computational setup.

3.1 A Brief Overview of Molecular Dynamics

Molecular dynamics simulations have wide ranging applications for analyzing the physics of a prescribed system. Many codes have been written to provide a platform for simulating behavior and properties of liquids, solids, and gases at the molecular scale. LAMMPS (Large-scale Atomic/Molecular Massively Parallel Simulator) is an example of such code, and will be used in this work to study interactions between graphene and yttria stabilized zirconia (YSZ).

LAMMPS is an open source code developed and maintained by Sandia National Laboratories, a US Department of Energy (DOE) laboratory. Distribution is readily available from the LAMMPS web page [40]. Once downloaded and compiled, the architecture of this code can be run in either serial or parallel, allowing for computational time to be optimized for a given circumstance. Many examples and tutorials exist to help

understand the scripting style and syntax of LAMMPS. For the work presented, the LAMMPS release from March 31 of 2017 was used.

3.1.1 Underlying Physics of LAMMPS

LAMMPS uses a variety of approximations and simplifications that reduce complexities, allowing for molecular interactions to be simulated. Atomic modeling is one such approximation, where the complexity of an atom can be simply depicted as a sphere with a point mass at its center. This reduces the intricacy of the molecular description and makes simulations tractable in a reasonable timeframe. Additionally, forces are associated between each atomic interaction to describe potential energy between surrounding atoms and molecules.

The physics used to describe the molecular behavior is founded upon Newton's equations of motion for collections of atoms, molecules, or macroscopic particles [41]. By treating each atom as a point mass, integration of Newton's equations with known positions, velocities, and interatomic potential forces allows for the time evolution of a system to be obtained. Throughout time integration, a wide array of properties can be quantified.

At the continuum scale, there are bulk equations that describe the conservation of mass, momentum and energy. When applied to a shockwave, these equations reduce to the Rankine-Hugoniot Equations, which are useful in analyzing the behavior of material consolidation. At the molecular scale, no such relationships exist, however, bulk properties can be obtained by integrating over a sufficiently large molecular volume. These simulations emulate the idealized dynamic behavior of bulk YSZ and graphene

systems with no porosity. Simulations can inform the necessary conditions for densification of the samples, map the thermodynamic response, and identify potential phase change of the molecular structures of the idealized structure.

3.1.2 Initialization, Running, and Visualization of LAMMPS Simulations

Prior to running a simulation in LAMMPS, an input deck and an atomic file must be prepared. Input decks are detailed codes which conducts the LAMMPS framework to perform desired studies. Typically, an input deck contains commands which allocate atomic potentials, describe domain dimensionality, state boundary conditions, specify simulation type, and log results from the ensemble. Input decks also reference atomic files to specify the ensemble's atom types, positions, and charges, and can be implemented into the code in a variety of ways. With all necessary components, the input deck can be executed in the LAMMPS framework.

Simulations can be run using a variety of platforms and processing techniques. For non-computationally intensive studies, simulations can be run locally using either serial or parallel processing. Computationally intensive studies, however, require high performance computing (HPC), utilizing greater computing power. Studies conducted in this work used Marquette Shock Physics Laboratory's high performance computer (HPC). Once runs are completed, visualization of the atomistic ensembles is needed. Visualization of the time integrated ensemble can be illustrated using multiple tools. AtomEye [42], VMD[43]–[49], and OVITO [50] are all high-quality visualization tools capable of illustrating atomic ensembles. This work utilized OVITO, illustrating the iterative evolution of the graphene and YSZ mixtures.

3.2 LAMMPS Simulations

LAMMPS requires material parameters be prescribed for an initial ensemble of atoms prior to any simulation. Once implemented, the collection of atoms must then be brought to equilibrium for ambient conditions. Additional processes such as shock compression can ensue following equilibration. Thus, simulations will proceed in two major steps: equilibration and shock compression studies.

Ensembles featured in this work were constructed using a MATLAB algorithm to orient and locate atoms. Lattice parameters for YSZ and graphene were input into the routine, and implemented based on a desired amount of unit cells of YSZ and graphene sheets. First, the algorithm accounted for desired graphene sheets, constructing the length and number of sheets. Graphene sheets were constructed in 2-D honeycomb structures, using a bond length of $c_g = 1.42\ \dot{A}$ and a triangular lattice constant of $a_g = 2.46\ \dot{A}$ [51] (Figure 3.1). Unit cells of 8%-mol cubic YSZ were then added depending on specified lengths, widths, and thicknesses. YSZ was constructed by first building zirconia unit cells. To satisfy the 8%-mol YSZ, oxygen atoms were then removed in the ensemble to form oxygen vacancies, and select zirconium atoms were replaced with yttrium. The lattice parameter and structure used for YSZ was $a_{YSZ} = 5.082\ \dot{A}$ (at 0 K) (Figure 3.1) [52].

Three constructed ensembles can be viewed in Figure 3.2, where an ensemble of YSZ, and two YSZ ensembles with graphene are illustrated. The YSZ ensemble was composed of 5,898 atoms, and had dimensions of $42.24\ \dot{A}\ x\ 42.24\ \dot{A}\ x\ 42.24\ \dot{A}$. The ensemble with one sheet of graphene was composed of 9,139 atoms, and had dimensions

of 55.38 $\dot{A}$ x 42.24 $\dot{A}$ x 50.41 $\dot{A}$. Finally, the ensemble with three sheets of graphene was composed of 9,907 atoms, and had dimensions of 58.52 $\dot{A}$ x 42.24 $\dot{A}$ x 50.41 $\dot{A}$. For both ensembles containing graphene, the sheets of graphene spanned the entire Y-Z plane. Results will emulate contact between two bodies of YSZ and the graphene, and will be representative of the physical interactions between the media.

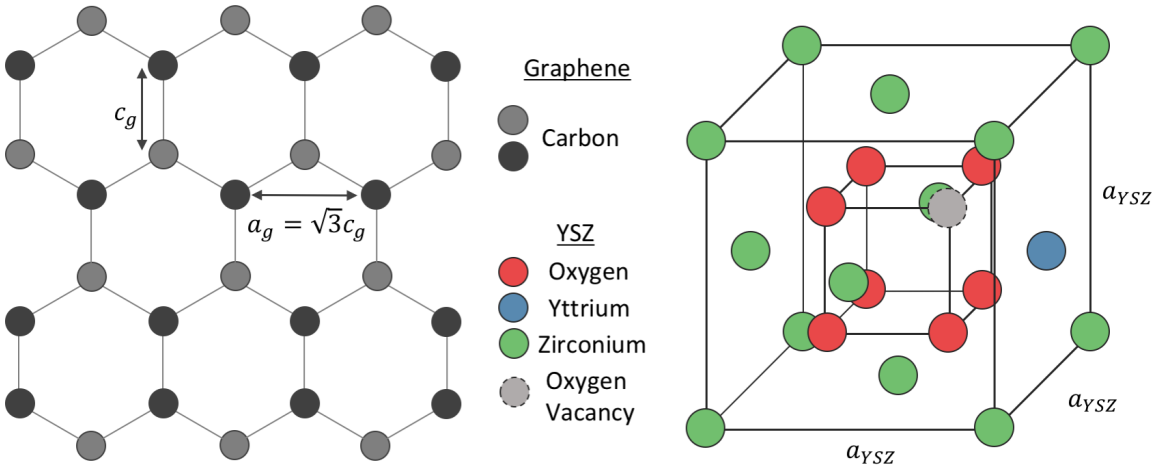

Figure 3.1: Atomic configurations for graphene and YSZ. The bond length of graphene used was $c_g = 1.42\ \dot{A}$, while the triangular lattice constant used was $a_g = 2.46\ \dot{A}$ [51]. The lattice parameter used for YSZ was $a_{YSZ} = 5.082\ \dot{A}$ at $T = 0\ K$ [52].

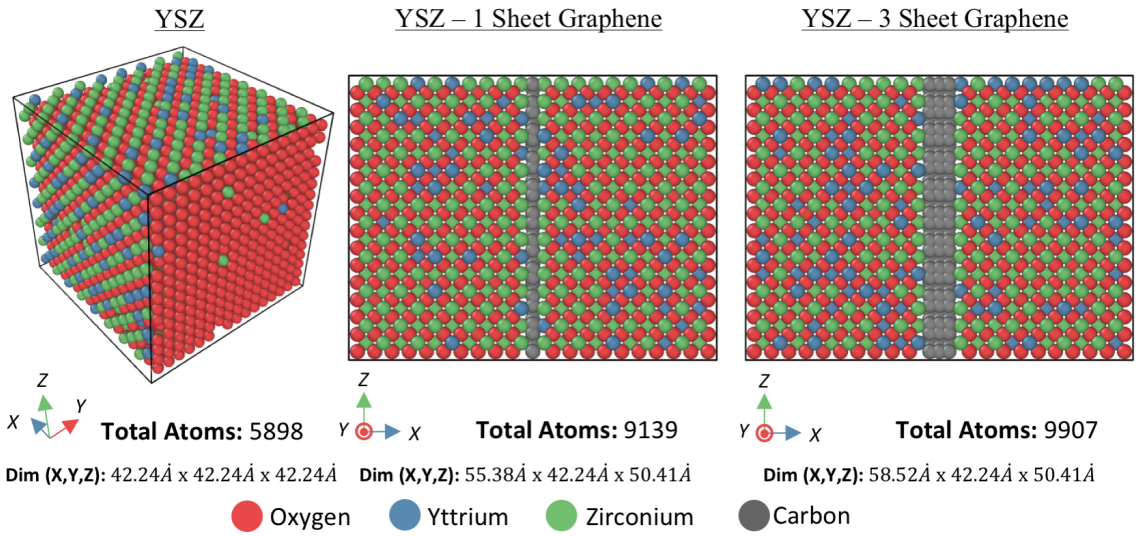

Figure 3.2: Ensembles constructed using the MATLAB algorithm. From left to right: YSZ, YSZ – 1 Sheet Graphene, and YSZ – 3 Sheet Graphene. The graphene sheet span the entire y-z plane.

As previously mentioned in Section 3.1.2, LAMMPS requires various input conditions for each simulation. Conditions pertinent to this study were: atomic weights, boundary conditions, force fields, and electrostatic interactions. Atomic weights used for each atom are specified in Table 3.1. Boundary conditions of each ensemble were declared as periodic, meaning atoms that exited a boundary of the ensemble re-entered on the opposite side of the ensemble. Two variations of force field models were implemented: The Coulomb-Buckingham model and the Lennard-Jones model. These models were chosen based off parameters existing in the literature for YSZ and graphene [52]–[56]. Formulas for each model are stated in Equations 3.1 and 3.2, and potentials are stated in Table 3.2. Stated potentials were found in the literature, or derived using the Lorenz-Berthelot mixing rules. Additionally, a cutoff distance of 10 $\dot{A}$ was applied to both force field models. Lastly, electrostatic interactions were handled using the Ewald summation technique. With the given information, ensembles were then initialized for equilibration.

Table 3.1: Atomic weights of elements used in LAMMPS.

Element	Oxygen	Yttrium	Zirconium	Carbon
Weight (amu)	15.9994	88.9059	91.2240	12.0107

Coulomb-Buckingham Potential:

$$\Phi_{ij}(r) = A_{ij}e^{-B_{ij}r_{ij}} - \frac{C_{ij}}{r_{ij}^6} + \frac{q_i q_j}{4\pi\epsilon_0 r_{ij}} \tag{3.1}$$

Lennard-Jones:

$$V_{ij}(r) = 4\epsilon_{ij}\left[\left(\frac{\sigma_{ij}}{r_{ij}}\right)^{12} - \left(\frac{\sigma_{ij}}{r_{ij}}\right)^{6}\right] \tag{3.2}$$

Lorenz-Berthelot Mixing Rules:

$$\epsilon_{ij} = \sqrt{\epsilon_{ii}\epsilon_{jj}} \tag{3.3}$$

$$\sigma_{ij} = \frac{\sigma_{ii} + \sigma_{jj}}{2} \tag{3.4}$$

Table 3.2: Lennard-Jones pair potentials and Buckingham pair potentials prescribed for the three ensembles.

Lennard-Jones Potentials			Buckingham Potentials			
Interaction	ϵ_{ij} $[eV]$	σ_{ij} $[\dot{A}]$	Interaction	A_{ij} $[eV]$	ρ_{ij} $[\dot{A}]$	C_{ij} $[eV \cdot \dot{A}^6]$
O - C [53]	0.00498	3.281	O - O [52]	9547.96	0.224	32.0
C - C [54]	0.00366	3.534	Zr - O [52]	1502.11	0.345	5.1
Y - C [55]	0.00093	3.473	Y - O [52]	1366.35	0.348	19.6
* Zr – C [54],[56]	0.00299	2.783	-	-	-	-

* Calculated using Lorentz-Berthelot Rules.

3.2.1 Equilibrium States

The equilibration process is illustrated in Figure 3.3 where a molecular composition of 8% mol cubic YSZ has been constructed in a domain with near perfect crystalline symmetry. Lennard-Jones and Buckingham pair potentials, cited in Table 3.2, have been implemented in the ensemble. Although the average potential energy and the density of the ensemble is correct, the distribution of energy across the molecular ensemble and crystallographic structure are not perfectly in equilibrium. Thus, the ensemble is integrated in time, allowing atoms to move, interact, and exchange energy to come to an equilibrium state that is more representative of the actual physical state. Time integration proceeds by minimizing the energy of the ensemble by iteratively adjusting atom coordinates to meet an energy threshold designated in the minimization algorithm.

Figure 3.3 presents the ensemble before and after equilibrium has been obtained. It can be noticed that atomic interactions have formed representative of the stable molecular structure for YSZ, and atomic energies have caused subtle relocation of the atoms. This process has then been repeated for two additional atomic ensembles containing graphene in Figure 3.4. Again, note the subtle relocation of atoms in the ensemble.

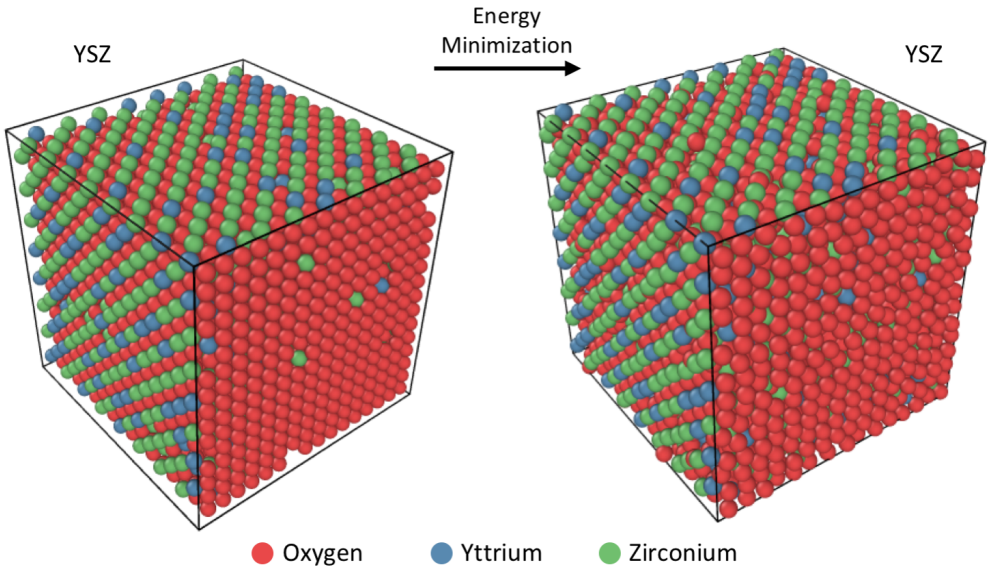

Figure 3.3: Minimization of energy between the initial and equilibrated state, where red, green, and blue atoms depict the oxygen, yttrium, and zirconium atoms in the simulated ensemble. Coordinates of each atom have been adjusted to minimize systematic energy.

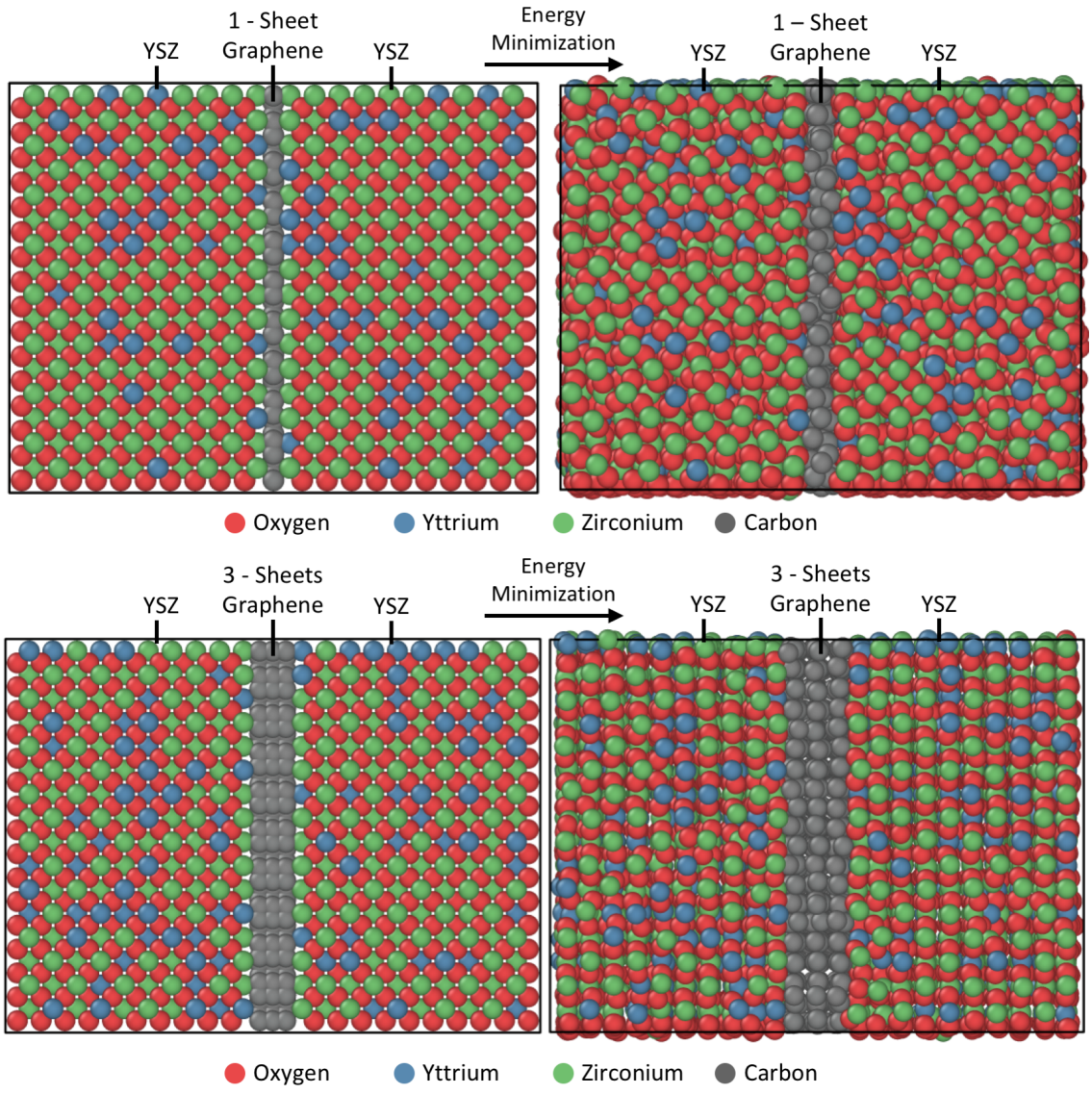

Figure 3.4: Minimization of energy between the initial and equilibrated state, where red, blue, green, and grey atoms depict the oxygen, zirconium, yttrium, and carbon atoms in the simulated ensemble. Coordinates of each atom have been adjusted in the far-right ensembles to minimize systematic energy between YSZ and graphene.

3.2.2 Shock Compression-Hugoniot Study

With equilibration performed, atomic ensembles were then subjected to shock compression. This work uses the Hugoniotstat method implemented in LAMMPS designed to satisfy the Rankine-Hugoniot jump conditions of a steady shock. Developed by Ravelo and colleagues [57], the method functions by compressing the ensemble while forcing the total temperature to remain on the bulk Hugoniot. This is accomplished by iteratively adjusting volume, and therefore pressure and energy, until a target temperature, T_t, is achieved and maintained. The following expression can be seen in Equation 3.5, where the variables P, v, e, N_{dof}, and k_B represent the pressure, specific volume, internal energy, degrees of freedom, and the Boltzmann constant. Within LAMMPS the function call is "nphug".

$$T_t - T = \frac{\left(\frac{1}{2}(P+P_0)(v_0-v)+e_0-e\right)}{N_{dof}k_B} = \Delta \mathrm{T} \tag{3.5}$$

Although time integration of the algorithm is not necessarily spatially or temporally correct during convergence, the end state of the compression is indicative of a Hugoniot state. Once converged, many material and thermodynamic properties can be quantified from the ensemble of atoms. Specifically, the relations of interest are the $U - u, P - \epsilon$, and $P - u$ planes. With this information, the shock response can be analyzed and related to the bulk response of a given material.

4 EXPERIMENTAL DESIGN AND SETUP

4.1 Introduction

The following section provides information on the impact experiments, and proceeds in three-fold. First, Marquette's light gas-gun and its functionality is described. Second, the process used for target design, target construction, and logistics of the experiment are detailed. Finally, the third portion of this section addresses diagnostics and data reduction.

4.2 Experimental Design

Marquette University's light gas-gun, seen in Figure 4.1, functions by accelerating a projectile using compressed gas. Pressure of the compressed gas is restrained by two burst disks up range of the projectile, which when released accelerates the projectile down the barrel. The projectile then impacts a target upon exiting the muzzle, orientated such that no free flight occurs. A target typically contains a sample or multiple samples of interest, and is violently impacted by the projectile. During the collision, the dynamic response of the sample(s) to shock wave loading is observed and recorded using three different diagnostics. A laser diode system, piezoelectric (PZT) pins, and photon Doppler velocimetry (PDV) are each used to study the velocity of the projectile, tilt of impact, and shock and particle velocity. Further explanation of the d-iagnostics can be found in section 4.3.1.

Once the experiment has ceased, it is often desirable to recover the impacted target for sample characterization. Recovery of the samples, however, demands that the target must be designed to withstand the rigorous loading conditions imposed by the collision. For these studies, design of a momentum trap and soft recovery system have been implemented in the design, and are detailed in the following section.

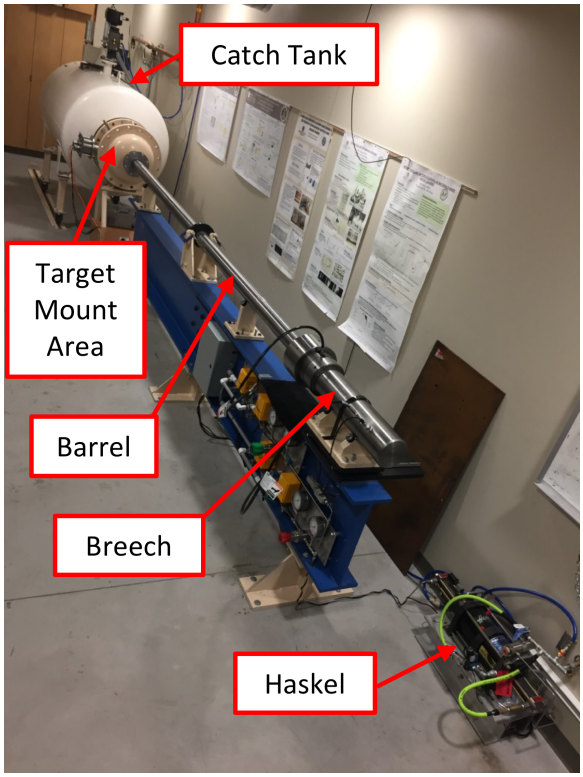

Figure 4.1: Marquette University Shock Physics Laboratory's 2-inch diameter light gas gun. Important components include a pneumatic pressure booster (Haskel), breech, barrel, target mount area, and the catch tank. Projectiles are loaded into the barrel, and high pressure contained in the breech is used to drive the projectile into the target located in the target mount area.

4.2.1 Optimization of a Momentum Trap

A technique employed in the literature for many shock compaction experiments integrates a momentum trap (also referenced as a spall plate) onto the downrange side of a target [27], [58]–[60]. Momentum traps have dual functionality, where employment enables a target to remain affixed, as well as deter strenuous tensile loading of the samples caused by rarefaction waves. Targets typically are constructed such that the momentum trap will displace from the target, "trapping" energy from the shocked system and reducing the tensile effects on the sample. A simple example of a momentum trap can be imagined by envisioning the mechanics of a Newton's cradle (Figure 4.2). When the chain of spheres is struck, pressure is induced at the impacted interface, and momentum transfer occurs. Over time, the last ball will eject from its original position conserving momentum. This same methodology can be employed for the design of targets, where the momentum trap acts as a mechanism to dissipate energy.

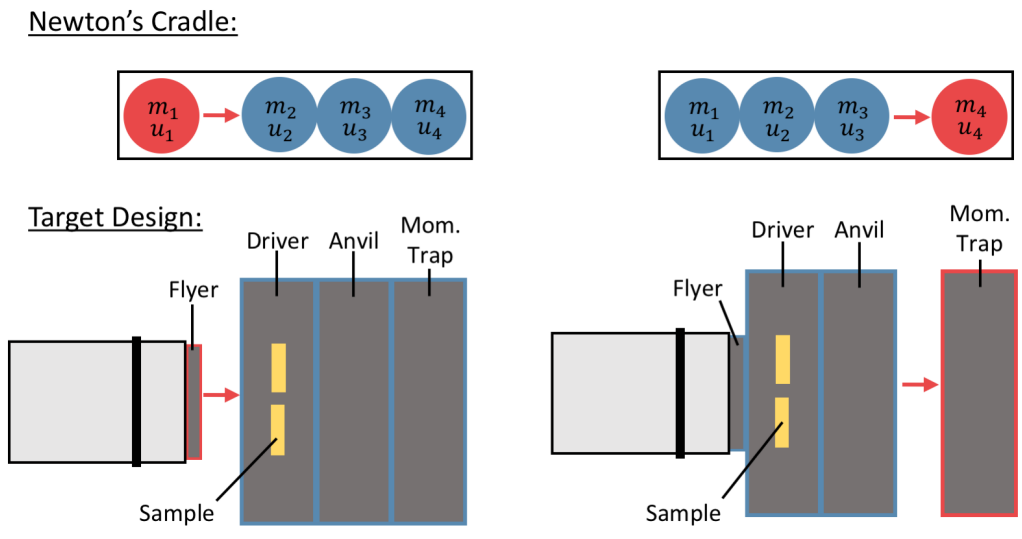

Figure 4.2: Illustration of the Newton's cradle, where the momentum transfer results in the ejection of the final mass.

As mentioned in Section 2.4, tensile effects imposed on the sample can fracture the consolidated sample. Proper implementation of a momentum trap can reduce the tensile effects imposed by rarefaction waves, however, design complexity arises because wave propagation requires multi-dimensional consideration. For this reason, CTH [61] was used to design and optimize the target. CTH is a multidimensional hydrocode which can be used to accurately model high strain rate phenomena such as a gas gun experiment.

While designing the target, work proposed by Schwarz et. al. [27] was considered. Schwarz proposed a theory detailing the importance of the duration of the shocked state and particle melting due to the primary shock pressure. Schwarz states the two conditions are mutually inclusive, where the time duration, t_d, of the shocked state influences the interfacial melting between the particulate. Parameters discussed indicate that a time duration of $t_d \cong 2\mu s$ is desired, as well as pressures, $P > 4.4\ GPa$. With these values in mind, target design can be optimized to satisfy these conditions.

The following diagrams presented in Figure 4.3 and Figure 4.4 depict results from the CTH simulation used to design the target for experiments. Zirconium was used as the sample in the simulation, while the target, momentum trap, and flyer were composed of steel. Although the materials used in the actual experiments differ slightly, well defined material properties exist within CTH for the materials used. Therefore, the following results are guidelines for what to expect experimentally, and may deviate experimentally due to specimen type, porosity, and heterogeneity. Figure 4.3A illustrates the initial state of the materials upon impact, while Figure 4.3B depicts the material deformation 12.9 microseconds after impact. In the simulation, the projectile located in the bottom half of

the simulation impacted the target at 320 m/s. The target and momentum trap were given no initial velocity, and can be seen in the upper half of the simulation with colors of gray and light gray. Figure 4.4A illustrates the particle velocity of the sample at two interfaces: the steel/sample interface and the PMMA/Sample interface. It can be noticed that a plateau of the particle velocity occurs for the sample/PMMA interface for approximately 2 μs. Also, a sudden rise in particle velocity can be observed from the PMMA/free surface. The sudden rise is important to note for later analysis of data, and is related to the release of the PMMA. Figure 4.4B depicts the expected pressure state of the sample. Notice the pressure state is maintained for approximately 2 μs at the steel/sample interface. Therefore, with the pressure being withheld for approximately two microseconds, this cross-sectional representation was used to design the target.

Table 4.1: Input properties of the target and projectile materials featured in the CTH simulation. Plot Colors are indicative of the target components in Figure 4.3.

Materials	EOS	Strength Model	Fracture (GPa)	X (cm)	Y (cm)	Color
Driv./Anv. - 304 SS	Mgrun 304_SS	JO Steel	-25.00	11.430	2.540	Dk.Gray
Mom. Trap - 304 SS	Mgrun 304_SS	JO Steel	-25.00	11.430	1.270	Lt. Gray
Sample - Zirconium	Mgrun Zirconium1	GKFRG Zirconium	-10.00	1.905	0.300	Yellow
Window - PMMA	Mgrun PMMA	VEP PMMA	-2.00	1.905	0.862	Lt. Blue
Flyer Plate - 304 SS	Mgrun 304_SS	JO Steel	-25.00	4.762	0.250	Lt. Gray
Projectile - PMMA	Mgrun PMMA	VEP PMMA	-2.00	5.003	9.999	Lt. Blue

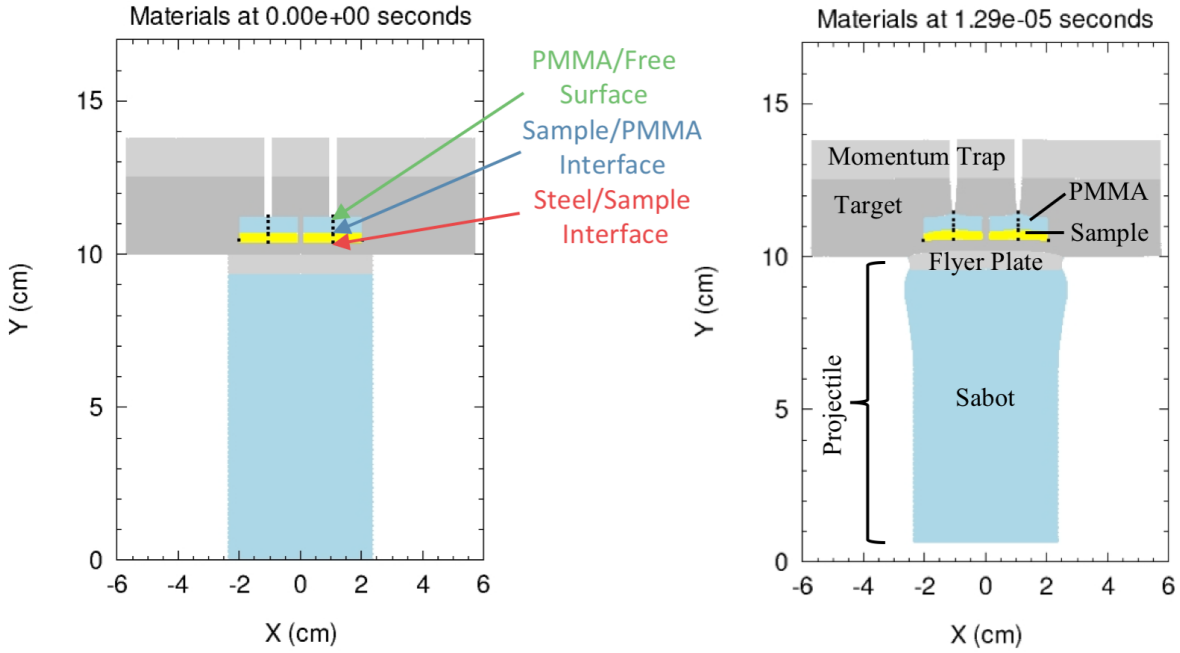

Figure 4.3: Illustration of the geometry simulated in CTH. A projectile impacts the target system where a sample, PMMA window, and momentum trap are incorporated in the design. Black dots indicate tracers, which record parameters of interest of a material in a finite area.

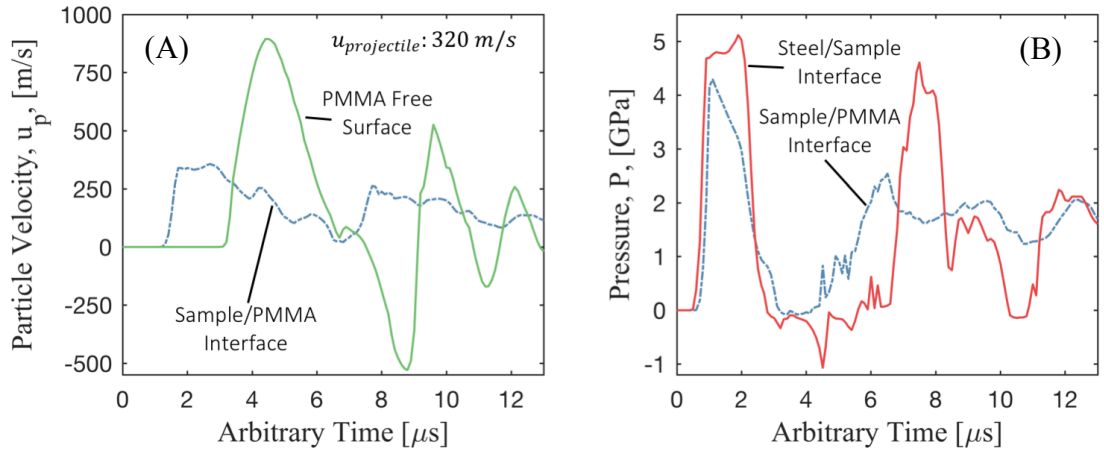

Figure 4.4: CTH simulations depicting (A) particle velocity and (B) pressure at various interfaces. Results are taken from tracers, which study a variety of parameters for a finite area. Tracers are indicated by the black dots in Figure 4.3.

4.2.2 Design & Construction of the Targets

Results determined from the CTH simulation aided in the design of the target. In addition to satisfying necessary loading conditions, another design objective was to make an easily manufactured assembly. It was decided that each target would contain the following components: an anvil, driver, momentum trap, four samples, four PMMA windows, and gasket materials. These materials play various roles, and allowed for easy assembly of the target with four samples. The following describes each component, their manufacturing process, and role in assembly.

Each target assembly was constructed out of three 1045 steel flats with a diameter of 4.50 inch (11.43 cm), and a thickness of 0.50 inch (1.27 cm). Each of the three flats have distinct purpose, functioning either as driver plate, anvil, or momentum trap. In the presented design, the driver plate and anvil embody the recoverable target capsule, while the momentum trap is used to dissipate energy and keep the target capsule together. Functionality of the driver plate in these experiments enables an interface to be struck by a flyer plate, as well as provide a region to pack a sample material into. The driver plate has four blind holes 0.75 inch (1.91 cm) in diameter and a depth of 0.35 inch (0.89 cm). A circular pattern of the four holes is positioned around the center of the circular plane, and four selected samples are packed into the driver. Eight threaded bolt holes (1/4 inch-20) and ten through holes are fabricated in the design. Threaded bolt holes fasten the anvil to the driver, and the through holes enable mounting of the target at the time of the experiment. Five additional holes are also fabricated for additional diagnostic hardware.

Design of the anvil has similar hole patterns to the driver plate. Purpose of the anvil is to fasten to the downrange side of the target, contain the samples, and remain

affixed throughout the longevity of the experiment. Like the driver, eight bolt holes and ten through holes are fabricated to anchor the target together, and mount the target in the experiment. Bolt holes were positioned such that they were a set distance away from the impacted region, allowing for material deformation to dissipate the tensile forces imposed on the bolts. Nine through holes are also fabricated around the center of the target to be used for diagnostic hardware.

Functionality of the momentum trap serves to dissipate energy from the target due to its downrange positioning of the anvil. Kinetic energy from the impact will propagate into the momentum trap, and cause the momentum trap to separate from the target capsule. Placement of the momentum trap on the target capsule is meant to eliminate the free surface from the downrange side of the anvil, keeping the threaded bolts in the driver/anvil affixed. Each momentum trap has nine drilled holes positioned to accommodate diagnostic hardware, as well as ten bolt holes used to mount the target.

Images and schematics for each target component have been appended to the following pages and in Appendix B. Figure 4.6 illustrates the machined target components, where it can be noticed that each target has been labeled in various manners. Labels are used for accounting purposes, and are utilized in the experimental data presented in Section 5. Each target component was assigned an identification number (i.e. Part No. 1 = Target 1's anvil, Part No. 2 = Target 1's driver, and Part No. 3 = Target 1's momentum trap), and each sample location was labeled numerically (i.e. Target 1: Samples 1-4, Target 2: Samples 5-8). PMMA windows, seen in Figure 4.6 were also labeled corresponding to its given sample location (i.e. Sample 1 = Window 1, Sample 5 = Window 5). Dimensions and weights were then recorded for each feature.

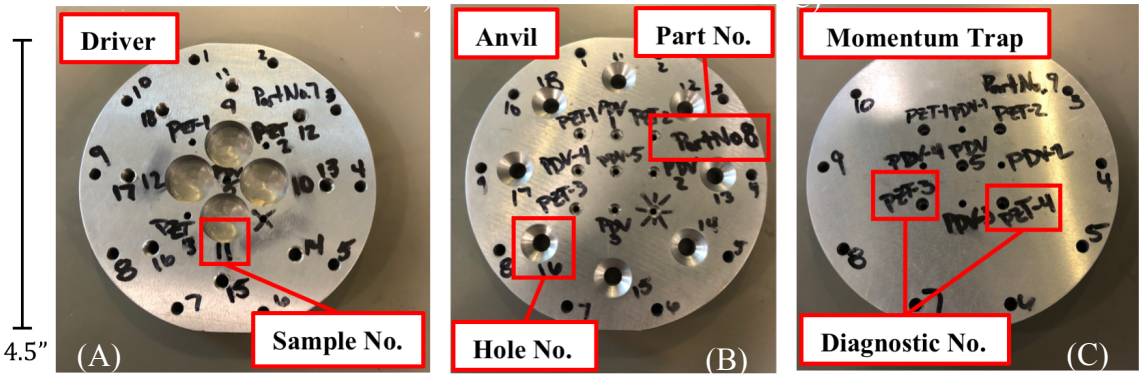

Figure 4.5: Components of the target assembly, where the (A) driver, (B) anvil, and (C) momentum trap are illustrated.

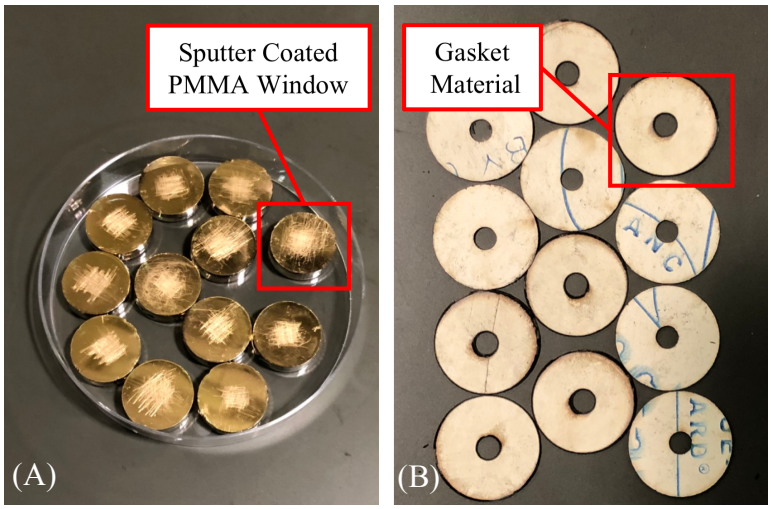

Figure 4.6: Components of the target assembly, where the (A) PMMA windows and (B) gasket materials are illustrated.

Construction of these targets required the use of Marquette’s Discovery Learning Center (DLC), Marquette University School of Dentistry’s (MUSOD) vapor deposition machine, and Marquette University’s Shock Physics Laboratory (MUSPL). The DLC was used to fabricate the target materials, which included the target/momentum trap,

projectile, and flyer plate. In addition, PMMA windows and gaskets were fabricated to fill the void space remaining from the sample.

PMMA windows allow for a transparent surface to be used to compress the sample. Using Marquette Dental School's vapor deposition machine (GSL-1100X-SPC12-LD), one side of the window was coated with gold palladium, making the surface reflective. Gold palladium provides a reflective surface which is critical for diagnostic purposes discussed later in Section 4.3.1.4. Gasket material (Garlock Performance 32000 Blue-Gard) was then placed between the PMMA window and the anvil to eliminate any remaining void space. Settings used for the fabrication of the PMMA windows, sputter coating of the windows, and fabrication of the gasket materials can be found in Table 4.2 and Table 4.3. With the PMMA windows and gasket materials in place, the anvil was fastened to the driver using eight 1 inch, ¼ inch-20 steel alloy bolts with 82 degree tapered heads, and 2-inch nylon bolts were used to mount the target to the mount plate in the gas-gun.

Table 4.2: Epilogue laser settings used to cut PMMA and the Garlock Performance 32000 Blue-Gard gasket material. Settings for speed and power the laser are in in percentages relevant to the maximum performance of the laser.

Material	Speed	Power	Frequency (Hz)
PMMA	6%	100%	5000
Gasket	20%	100%	1000

Table 4.3: Vaper deposition settings used for the GSL-1100X-SPC-12 compact Plasma Sputter Coater. The fit equation used to calculate the sputtered thickness is $D = KIVt$.

Sample	Pressure (Pa)	Sputtering Constant, K	Current, I (mA)	Voltage, V (kV)	Time, t (s)	Sputter Thickness, D ($\dot{A}$)
PMMA	6	0.17	10	1	210	357

4.2.3 Test Materials

Materials tested in this work are various mixtures of graphene and YSZ. In total, eight different compositions of the materials are studied, where two control variables are tested: YSZ particle size and graphene weight percentage. YSZ was sourced from Skyspring Nanomaterials Inc. (8532QI), and it was found that the size of particles for the nano-YSZ and micro-YSZ were ~20 nm and ~700 nm, respectively. Additive mixtures were formed with graphene nanomaterials and the YSZ specimens by Oceanit. Various weight percentages of graphene were added (0%, 1%, 3%, 5%) to the different particle sizes of YSZ. Table 4.4 contains a breakdown of the weight percentage and mole percentage of the various mixtures.

Table 4.4: Weight percentage and mole percentage breakdown of the mixed specimens

YSZ		Graphene	
Weight Percentage (Wt. %)	Mole Percentage (Mol %)	Weight Percentage (Wt. %)	Mole Percentage (Mol %)
100	100	0	0
99	77	1	23
97	53	3	47
95	39	5	61

Pertinent measurements of the powdered samples used in experiments can be found in the Appendix A under Table 6.2. The average weight of the samples was 1.8238 g with a standard deviation 0.0587 g, and the average initial bulk density of the samples was 2.9979 g/cc with a standard deviation of 0.3275 g/cc. Density of the packed nanometer grain size samples were generally smaller in magnitude than the density of the micrometer grain size packed samples.

4.2.4 Target Assembly

Prior to compaction studies, targets must be prepared to encapsulate the given samples. As mentioned previously, each target was first labeled, and weights and dimensions were recorded for each critical component. Once measured, each target was cleaned to eliminate any residual materials where samples were packed. Samples were then weighed, and poured into designated regions of the target. PMMA windows were then placed such that the sputter coated surface would be in contact with the samples, and pressed into place using a pneumatic press to a hydraulic pressure of 4,000 psi (area of PMMA window = 0.75 inch). With all samples pressed, the anvil was attached to the driver, and placed on a vibrational table for ten minutes in an attempt to minimize porosity. Windows were pressed again, and gasket material was placed in the void space between the PMMA window and the driver. The anvil was then attached to the driver.

Once completed with the pressing of the samples, PDV collimators and PZT pins were then placed into the target. Each PDV collimator and PZT pin was positioned in the target such that light return for the collimators was (>-35 dBm) and the PZT pins had slight protrusion from the impacted surface (~1mm). Protrusion was measured with coordinate measurement machine (CMM) (Brown and Sharp). Each diagnostic component was then glued into place using a fast-acting adhesive (Loctite 1363589), and followed with epoxy (Hardman 04001) for strength. Additionally, epoxy (Hardman 04001) was applied to each bolt of the target and the interface between the anvil and momentum trap. Such precautions were taken to alleviate free surfaces between the bolts and the target. With completion of the stated procedures, PZT pin protrusion was measured with the CMM, and the target was mounted in the gas gun.

4.2.5 Design and Construction of the Projectile

Projectiles used in these experiments were designed to have two significant components, the sabot (projectile body) and the flyer plate (impactor). When assembled, the projectile package is loaded into the light gas-gun, and driven down the barrel using high pressure gases. The following details the components, construction process, and assembly for the projectile.

Design of the sabot is intended to minimize the weight of the assembled projectile, allowing for higher velocity to be achieved with lower breech pressures. Each sabot was fabricated out of polycarbonate, which is a highly durable material used in many ballistic applications. Use of polycarbonate and the placement of a countersunk hole in the rear end of the projectile enabled mass reduction. Critical dimensions of the sabot are the diameter and countersunk hole used to press fit the flyer plate. The diameter of the sabot is slightly undersized (1.97 inch or 5.07 cm) relative to the barrel (2.00 inch or 5.08 cm), while the countersunk hole has a diameter of 1.87 inch (4.75 cm). It can be noticed that there are two locations on the shaft of the sabot which have a smaller diameter in the design. Buna O-rings were placed in these locations, sealing air from escaping around the projectile. In the front of the projectile, a flyer plate composed of 1045 steel was mounted with a thickness of 0.30 inch (0.76 cm) and a diameter of 1.87 inch (4.75 cm). The flyer plate served as the surface that will impact the target, and was be ground to be planar.

Assembly of the projectile required the following progressions. First, critical dimensions of the sabot were measured using the CMM machine and a Vernier caliper. Second, a minute amount of epoxy was placed in the contact area between flyer plate and

sabot, and the flyer plate was press fit into place. The projectile was then positioned such that the flyer plate was facing upwards, and a weight was placed to deter the flyer plate from being displaced as the epoxy cured. Once the epoxy was cured (~1 hour), the CMM was then used to measure the perpendicularity between the flyer plate and the sabot. Buna O-rings were then positioned on the sabot, light vacuum grease (Dow Corning 146355D) was applied to the O-rings, and the projectile was then ready to be inserted into the barrel of the gun. Images of the components and assembly process can be viewed in Figure 4.7.

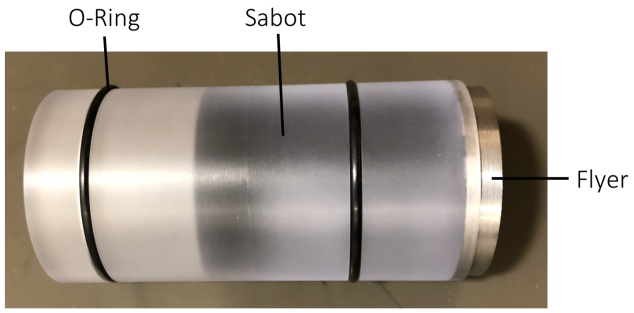

Figure 4.7: Assembled projectile used in experiments. Note the cavity on the left side of the sabot. Reduction of mass in the projectile was achieved through the cavity

4.3 Instrumentation, Data Acquisition, and Data Processing

Impact experiments use many diagnostic instruments to acquire critical results from an experiment. Additionally, collected data requires processing to unravel the state achieved within an experiment. The following subsections aim to detail the equipment and techniques used in the experiments, proceeding into the methods used to reduce data.

4.3.1 Diagnostics, Data Collection, and Data Processing

Three diagnostics are used to collect data pertaining to the velocity of the projectile, planarity of impact, and the particle velocity observed for a given material. In the given arrangement, a laser diode system, piezoelectric (PZT) pins, and photon Doppler velocimetry (PDV) are used to collect the stated information. Each data set is interconnected, and is critical for data processing. The following outlines the functionality of each system, an example signal, and the calculations performed to determine the various parameters.

4.3.1.1 Laser Diode System

The laser diode system allows for projectile velocity to be measured prior to impact. Located at the end of the barrel, four laser diodes and four photodiodes comprise the system (Figure 4.8). Each laser and photodetector is paired and aligned perpendicular to the flight path of the projectile. When the laser plane is obstructed, the output voltage from the photodetector is decreased. This reduction in voltage indicates the projectiles location at an instance in time. With the measured distances between the laser planes, a velocity can be calculated.

Processing of a collected signal requires the analysis of the voltage drop observed for each laser plane. For discussion, a sample signal has been included in Figure 4.9. In the figure, four signals are resolved for each plane. With each drop, associated time instances, t_i, and known distances between diode planes, dx_i, can be used to determine a projectile velocity. The subscript, i, denotes the diode plane number, where the total

number of planes is denoted by I. Distances between diode planes are approximately 0.75” (1.91 cm), and are measured before each shot. Therefore, determination of the time instance for voltage drops, and accurate measurement of the distances between each plane is quintessential for the data processing.

Determination of a single t_i for each channel can lead to erroneous results because of gradient variance for each voltage signal. Projectile velocity calculations performed in this work aim to remedy by calculating velocities over a range voltage percentages, l_n, with associated time instances t_{i,l_n} for a total number of calculations of L. Velocities are calculated using known distances between the two lasers, and the time difference between corresponding time signals. Equation 4.1 denotes the expression used to calculate projectile velocity. A MATLAB algorithm has been implemented which determines projectile velocity, as well as the uncertainty in the measurement. Black lines seen in Figure 4.9 indicate calculations performed on the signal using the MATLAB algorithm.

$$u_{projectile} = \frac{1}{L(I-1)} \sum_{i=1}^{I-1} \sum_{l=l}^{L} \frac{dx_i}{\left(t_{(i+1,l_n)} - t_{(i,l_n)}\right)} \tag{4.1}$$

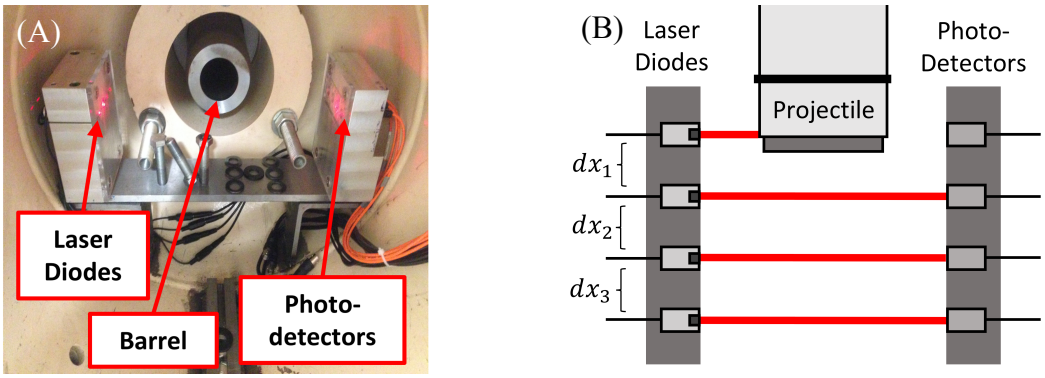

Figure 4.8: Images of the laser diode system used to measure projectile velocity. Figure 4.8a [62] depicts the physical system, while Figure 4.8b depicts the projectile eclipsing the first laser plane.

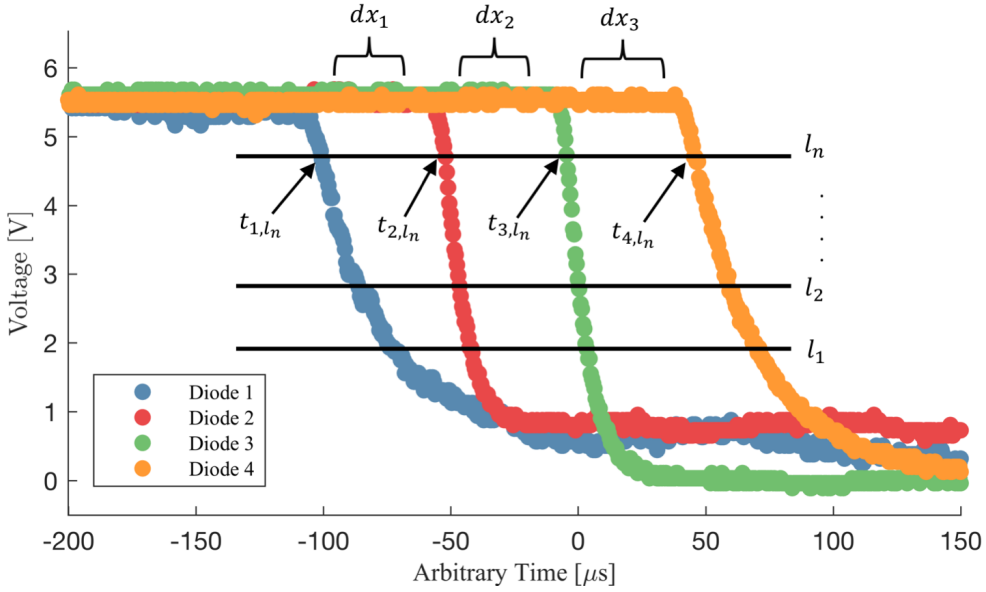

Figure 4.9: Sample signal resolved using the laser diode block. Various colors depict the signal observed by each laser diode. The sudden decrease in voltage indicates the diode plane has been obstructed by the projectile.

4.3.1.2 Piezoelectric (PZT) Pin Setup

Piezoelectric (PZT) pins (Dynasen 0.093" dia. CA-1136) enable measurement of the planarity of impact between the flyer plate and the driver. Each PZT pin is a thin

brass cylinder that has a piezoelectric crystal positioned in the cylinder's face (Figure 4.10). Crystals are positioned to be impacted by the projectile, and output a large voltage (~70 volts) when struck. The pins were connected to a Dynasen pin mixer (Model CS2-50-300), which initialized data collection on an Agilent DSO6054A (4 GS/s, 500 MHz) oscilloscope. For all experiments, the acquisition rate of the oscilloscope was 4 GS/s. With acquired data, planarity of impact is determined using multiple PZT pins, forming an impact plane from arrival times in the signals. With planarity of impact, known instances of the shock arrival to the samples can be calculated. This will be further discussed in the following section.

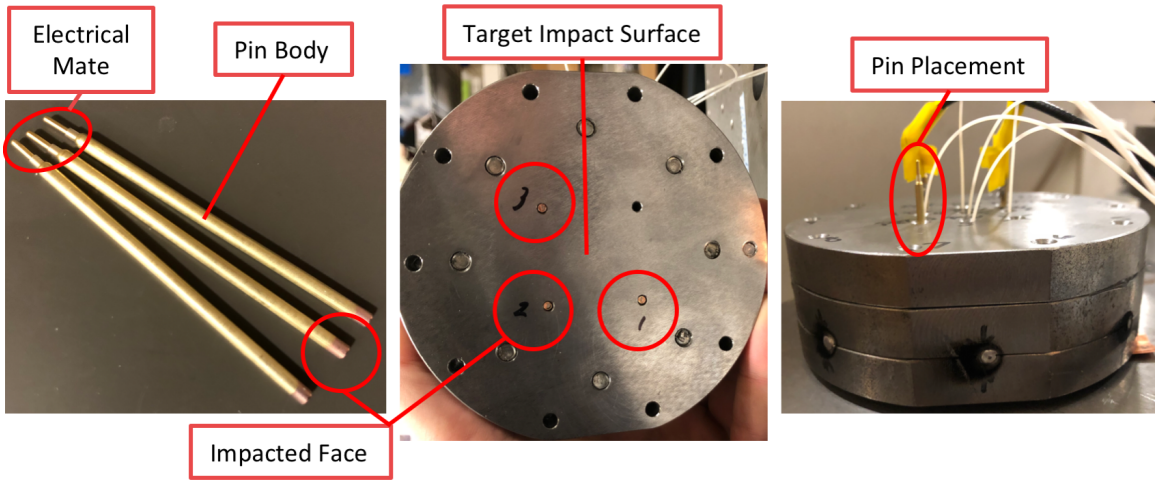

Figure 4.10: PZT pins used in this work, where anatomy and placement have been illustrated.

This work utilizes an arrangement of three PZT pins, which can be seen in Figure 4.10. Each PZT pin was wrapped in insulation tape, and a BNC cable was either soldered or connected to the pin. Pins were then placed into the target, where the target had been elevated slightly (~0.4 mm) to allow for slight protrusion of the pin face from the face of the target. Epoxy (Hardman 04001) was applied to the exposed shaft on the downrange

side of the PZT pins, and allowed to cure for at least one hour. Measurements of the protrusion were made utilizing a CMM device, and were used in the data processing.

Data analysis performed for the PZT pins is a function of three linear planes; the flyer plate (p_1), the three PZT pins (p_2), and the driver (p_3) (Figure 4.11). With known projectile velocity and plane of pin protrusion, the plane of the flyer plate can be defined and used to calculate the tilt angles (dihedral angles) θ_2 and θ_3 between the intersecting planes. Equations 4.2 and 4.3 state the general nomenclature used to define the plane and associated normal vector, while Equation 4.4 is the methodology used to calculate the dihedral angle, θ_m, between two intersecting planes.

A MATLAB routine has been developed to calculate and visualize the impact between the flyer plate and the other planes (Figure 4.12). In the far-left images, a magnified visual can be seen for the flyer plate (red), PZT pins (black), and the target plane (blue). Middle images depict a top down view of the flyer plate, PZT pins, and target. Far-right images depict corresponding signals indicating the impact of the PZT pins. Note the rise in voltage as the pin is impacted. Flyer and PZT impacts have been circled in light green, and a color gradient can be noticed when the flyer intersects the target plane.

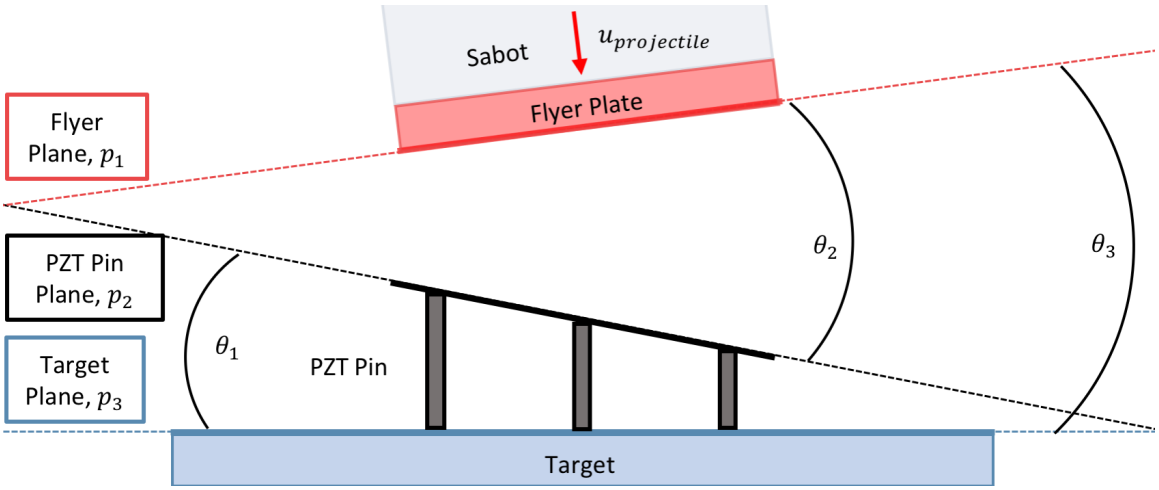

Figure 4.11: Illustration of the planes used to determine tilt. Angles are exaggerated for depiction purposes.

$$p_j = f(x_j, y_j, z_j) = a_i x_j + b_i y_j + c_i z_j + d \tag{4.2}$$

$$\hat{n}_j = (a_j, b_j, c_i) \tag{4.3}$$

$$\cos\theta_m = \frac{\hat{n}_j \cdot \hat{n}_k}{|\hat{n}_j||\hat{n}_k|} \tag{4.4}$$

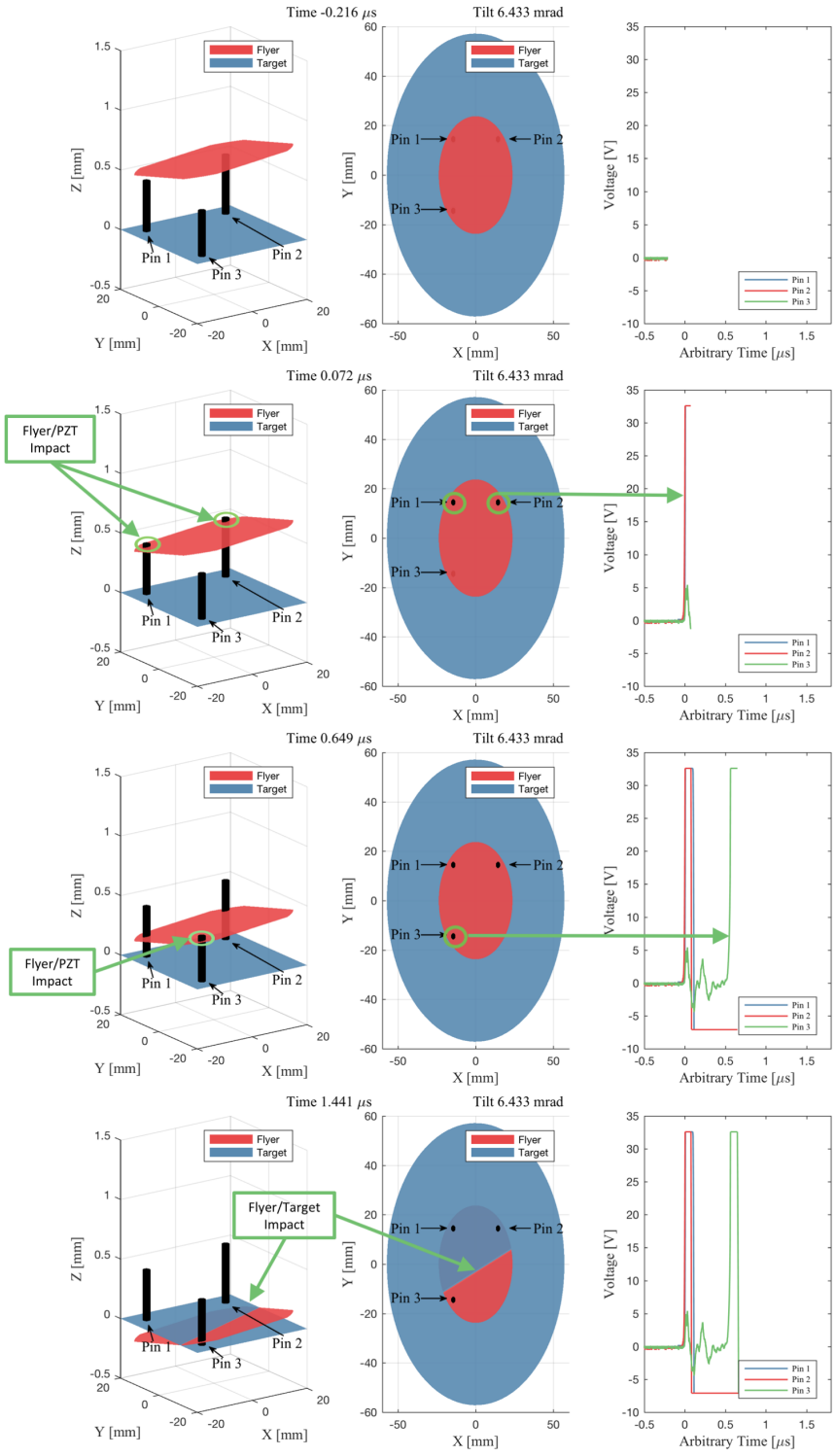

Figure 4.12: Illustrations of the flyer plate plane (red) impacting the PZT pins (black) and the target plane (blue). Far-right plots depict the resolved signals from the impact of PZT pins, where sudden rise in voltage indicates the pins have been impacted.

As mentioned, reduction of PZT pin data gives informative results regarding the tilt angle and impact times between various locations of the flyer plate and target surface. Progressing forward, known information about the impact times are utilized to determine tilt corrections which can be used to calculate transit times of the shock waves through the materials. This is performed by implementing tilt corrections to mitigate differences in arrival time in the PDV traces, and allow for shock velocities to be quantified.

4.3.1.3 Tilt Corrections

Tilt corrections are necessary for accurate arrival times of the shock waves to be observed. Defining the plane of flyer plate and the projectile velocity allow for the time of impact to be calculated at specified locations in the plane. Operations were performed for the spatial locations of the PZT pins to collapse the impact of the PZT pins onto each other. Additionally, this step was performed for the velocimetry diagnostics in the following sections, and will be further discussed in section 4.3.2.

4.3.1.4 Photon Doppler Velocimetry (PDV) System

Photon Doppler velocimetry (PDV) is utilized in this work to acquire highly resolved particle velocity for a given surface. PDV systems function as a Michelson interferometer, where a Doppler frequency shifted target light, f, is combined with a reference light that has a steady frequency, f_o [63]–[71]. Combination of these two frequencies, known as a differential beat frequency, f_b, is indicative of an apparent velocity. Equation 4.5 [63] depicts the fundamental relationship between an apparent

velocity and beat frequency, which is used to calculate particle velocity from experimental measurements.

In shock experiments, frequency shifted light is a product of placing a collimated laser probe (collimator) incident on a material surface. As the shock wave reaches the incident surface, a frequency change is measured by the PDV system, and recorded using an oscilloscope. Various systems have been constructed to obtain velocity measurements, however Marquette's PDV is a traditional heterodyne PDV system [72]. A schematic of the components which comprise Marquette's PDV can be found in Figure 4.13, as well as an image of the system and a collimator (AC Photonics, 1550 nm, 1CL15P006LCC01, FC/APC).

$$v^* = \frac{\lambda_o f_b}{2} \tag{4.5}$$

Each target featured five PDV collimators. Collimators were positioned and epoxied to observe various surface velocities within the target, and can be seen in the cross-sectional representation of the target in Figure 4.14. Four collimators were positioned incident on the downrange side of samples on the sample and PMMA interfaces, while one collimator was positioned incident on a steel interface. The collimator incident on the steel was observing particle velocity at a depth comparable to the up-range side of the samples. Positioning of the collimators in the described manner measured when the shock wave arrived at the front and back of the samples. Calculations were performed using the physical depths of surfaces and rise times of signals.

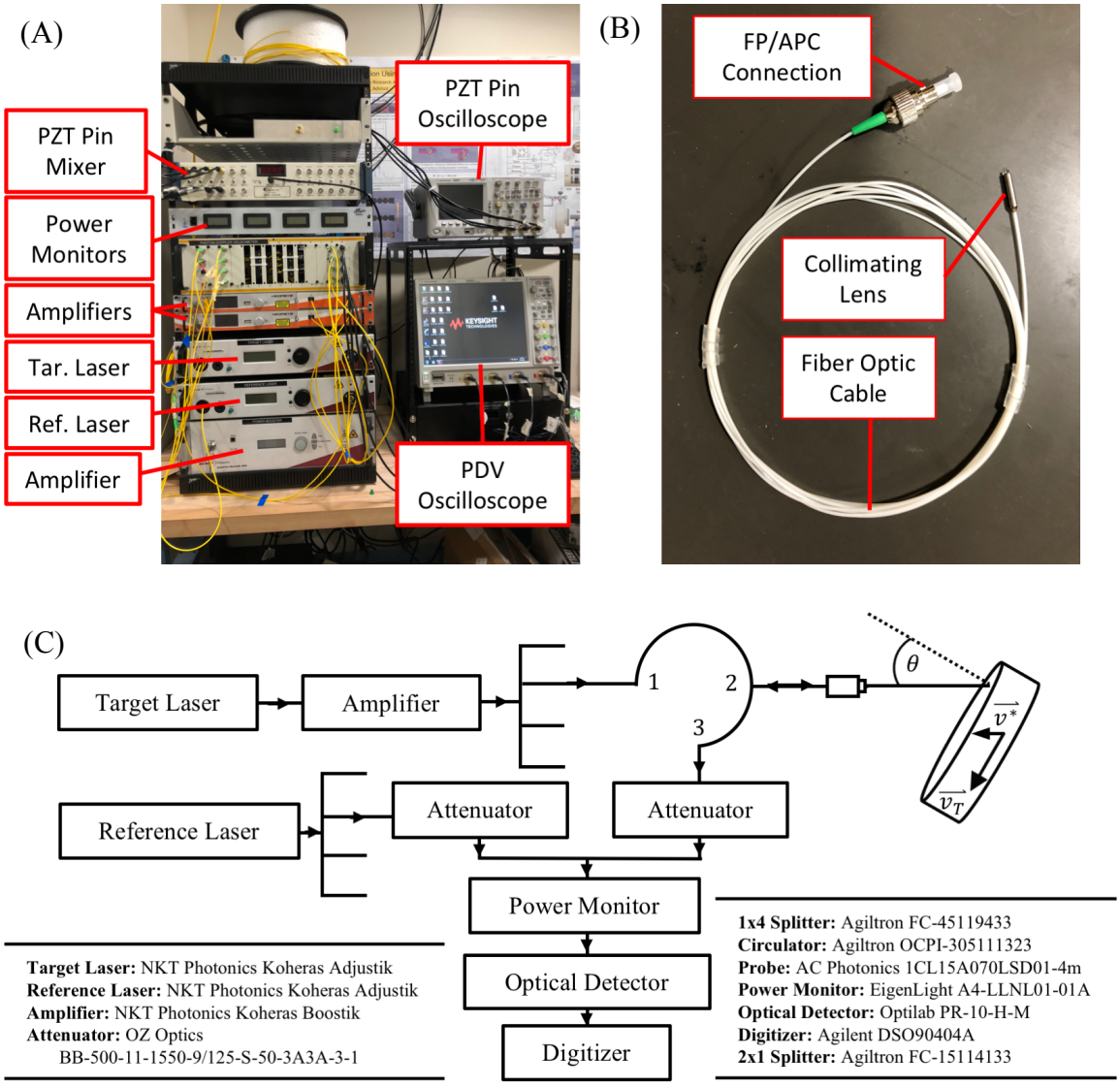

Figure 4.13: Illustrations of (A) Marquette University's PDV system, (B) the fiber optic collimators used in this work, and (C) the internal components of Marquette's PDV [72].

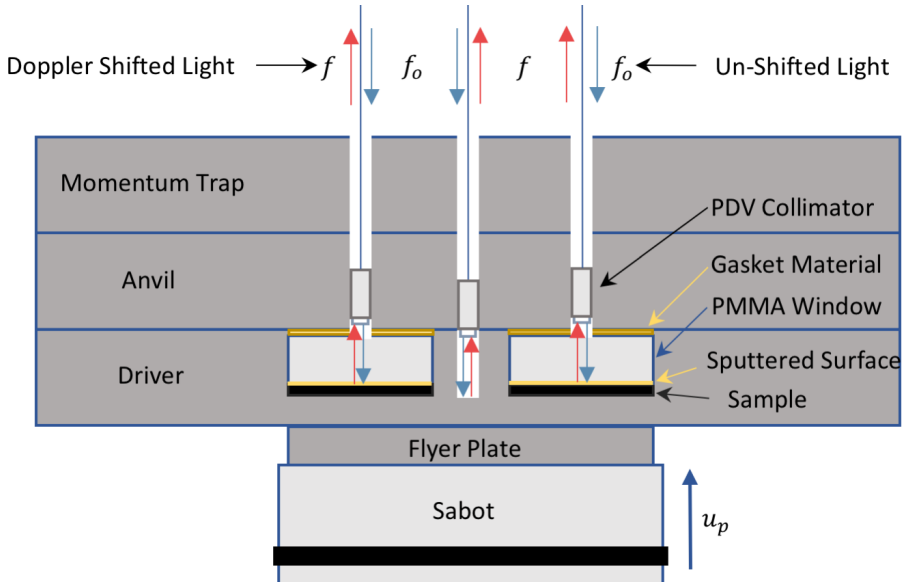

Figure 4.14: PDV placement within a target. Un-shifted light (light-blue arrows) and Doppler shifted light (red arrows) are emitted and captured using the collimators.

Data reduction of PDV signals performed in this work utilizes PlotData [73], a software developed at Sandia National Laboratories. PlotData employs a short-time Fourier transform (STFT), which is used to determine resulting beat frequencies over local sections of a signal. Such techniques are advantageous for detecting temporal changes in frequency. A resulting spectrogram and trace of the reduced data can be seen in Figure 4.15, where pertinent settings typically used in PlotData are a time/slice of 7.50 nanoseconds and a velocity/bin setting of 0.236 m/s. These settings define the size of the local sections analyzed in the signal, as well as the precision of the frequencies calculated.

It can be seen in the spectrogram of Figure 4.15 that two distinct traces are present. Recall CTH simulations performed on the target configuration in Figure 4.4. It can be noticed in both the CTH simulation and the experimental data that there is a

plateau indicative of the Hugoniot state of the material and a particle velocity indicative of the release of the PMMA window. It is believed that both velocities were observed by the velocimetry technique simultaneously once the wave reached the free surface of the PMMA window, hence the presence of two velocity traces in the spectrogram between three and five microseconds. Consideration and caution were taken in data reduction to ensure the reduced trace did not contain the free surface release.

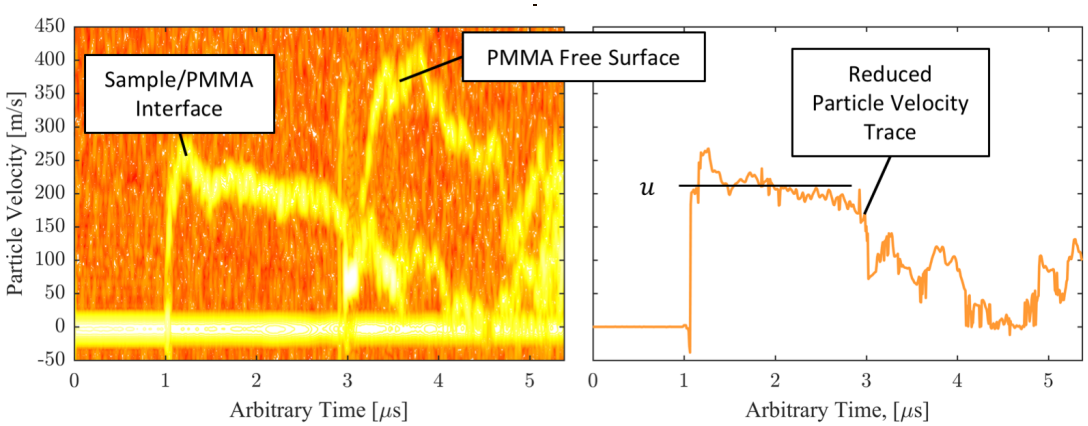

Figure 4.15: PDV signals reduced using PlotData. Illustrated STFT results can be seen in the spectrogram on the left, and the reduced trace on the right. CTH simulations indicate that the trace that reaches ~400 m/s above is the free surface of the PMMA window.

Spectrograms and traces were resolved and reduced for each of the five collimators featured in a target configuration. As mentioned previously, four signals were resolved for sample/PMMA interfaces, and one signal was resolved for the steel interface at the same depth as the up-range portion of the samples. With reduced PDV signals, time corrections were then applied to determine shock and particle velocities.

4.3.2 Time Corrections

With known tilt of impact, time corrections can be applied to the reduced PDV traces to shift the arrival time. Time corrected signals, seen in Figure 4.16, enable for transit times of the shock propagation through steel, t_{steel}, as well as transit time through the sample, t_{sample}, to be determined. Known sample thicknesses were used to determine the shock velocity for each sample, and used to impedance match with the projectile velocity to determine various Hugoniot properties. It is important to note the implications time corrections have in the calculation of shock velocities through the samples. Without correction, erroneous shock velocities may be calculated.

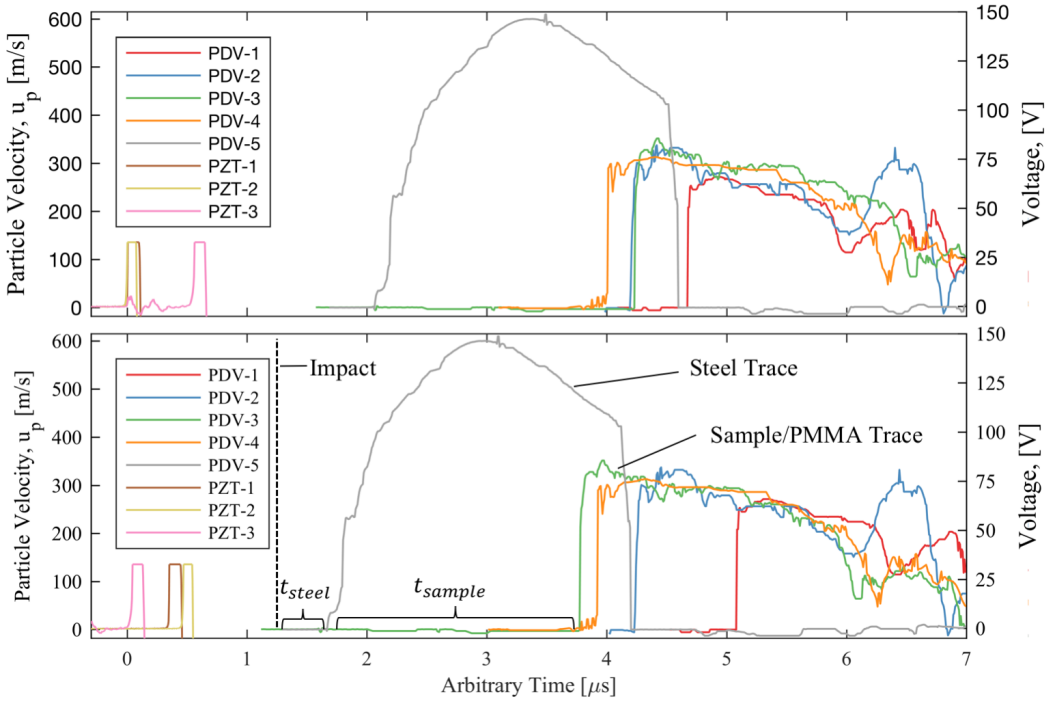

Figure 4.16: Raw and time corrected PZT and PDV signals in the upper and lower plots respectively from a single test series. Displacement of the raw signals due to time corrections can be noticed in the lower plot. Transit times associated with propagation of the shock waves through the steel and samples are denoted by t_{steel} and t_{sample}.

5 COMPUTATIONAL AND EXPERIMENTAL RESULTS

The following sections bridge computational and experimental results in the following way. First, molecular dynamics results are illustrated comparing results between ensembles. Second, experimental data is presented. Finally, the two data sets are contrasted, and the implications of porosity and added graphene are discussed.

5.1 Molecular Dynamics Simulations

The following images and figures depict results for the three ensembles studied using the Hugoniotstat method, described previously. The first setup, seen in Figure 5.1, analyzed an ensemble of YSZ. This was followed by the addition of one or three graphene sheets between lattices of YSZ (Figure 5.2). The Hugoniotstat algorithm compressed the ensembles using the Langevin piston method to maintain constant uniaxial pressure, while iteratively adjusting the temperature and volume to stay on the bulk Hugoniot. Compression of the ensemble was performed for 10 picoseconds (10^{-11}sec) with a one femtosecond (10^{-15}) time step. A series of 60 computational studies were performed on each of the equilibrated ensembles spanning pressures between 0.1 GPa to 20 GPa. Figure 5.1 and Figure 5.2 illustrate the ensembles under 6.33 GPa of pressure, while Figure 5.3 displays the Hugoniotstat methodology. Convergence of a solution can be seen in Figure 5.3 in the center of the swirl pattern. Even though the end state converges on the Hugoniot, this figure clearly illustrates the path taken by the Hugoinotstat function is not a Rayleigh line. For all Hugoniot parameters, the values

were calculated using the converged state. The resulting $U - u$, $P - \epsilon$, and $P - u$ relations can be viewed in Figure 5.4.

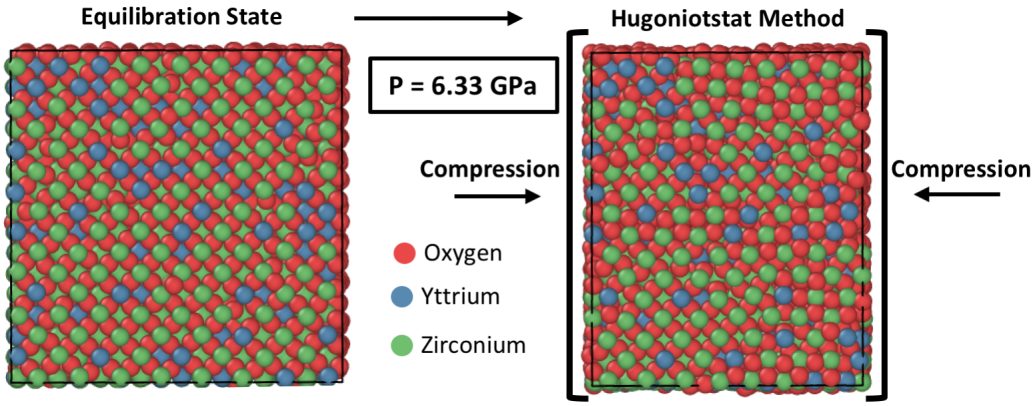

Figure 5.1: YSZ ensemble (2D slice) studied under uniaxial compression, where the atomic colors red, blue, and green depict the oxygen, yttrium, and zirconium atoms in the simulated ensemble. Black brackets indicated the compressed direction.

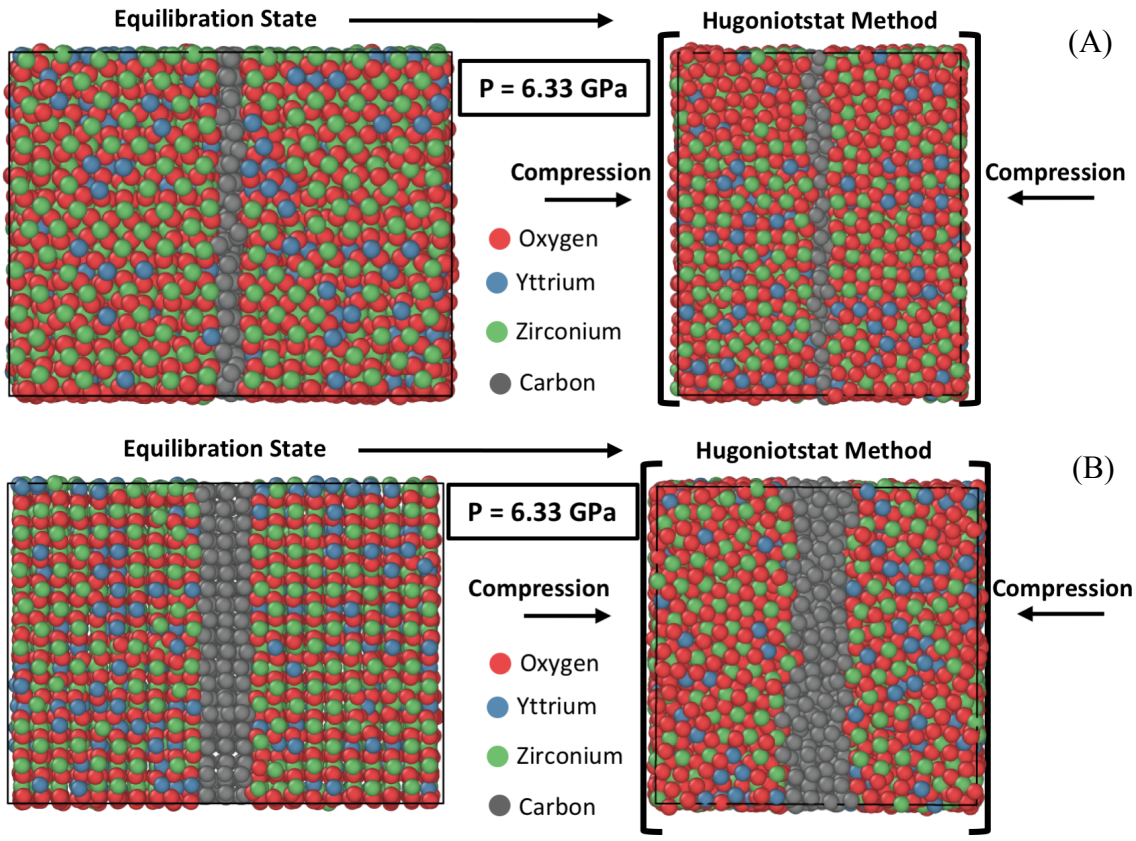

Figure 5.2: Graphene and YSZ ensembles studied under shock loading, where the atomic colors red, blue, green, and grey depict the oxygen, zirconium, yttrium, and carbon atoms in the simulated ensemble. Black brackets indicated the compressed direction. (A) Depicts one sheet of graphene between YSZ. (B) Depicts three sheets of graphene.

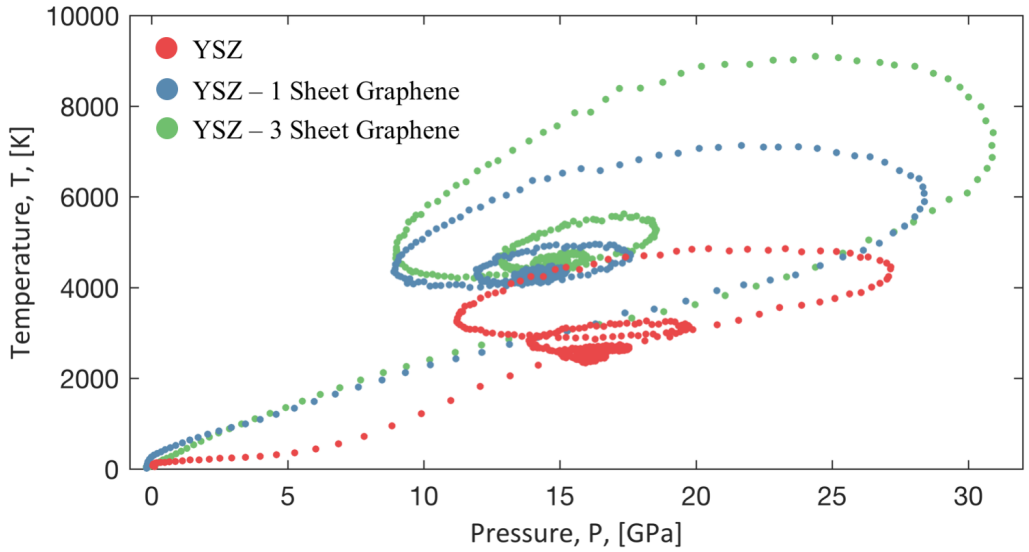

Figure 5.3: Illustration of the Hugoniotstat method, where the iterative functionality of the algorithm is presented. Convergence of the algorithm is depicted by the swirl pattern.

Figure 5.4 depicts the Hugoniot planes calculated in LAMMPS for three ensembles. First, focus is placed on the $U - u$ plane, where observations can be made regarding non-linearity of the curves and implications of graphene content. In the $U - u$ plane, non-linear behavior is observed between 800-1,500 m/s for all ensembles (Figure 5.4A). Note the similar behavior observed in experimental data published by Mashimo [15] for cubic YSZ. Mashimo hypothesizes that the non-linear behavior is indicative of phase change from cubic YSZ. Although there are apparent similarities in the data, conclusive statements cannot be made regarding phase transitions in the MD simulations.

A few general remarks can also be made regarding the implications of graphene. As graphene content is increased in the ensemble, it is observed that the resulting shock velocity is decreased for the structures. This can possibly be explained by impedance differences in the medium, where graphene has a lesser impedance than YSZ. Another observation to note is that as particle velocities exceed 1,500 m/s, the three ensembles begin to converge to similar shock velocities. This may be indicative of impedance changes in the YSZ to closer to that of graphene, which would provide one possible explanation as to why the addition of graphene reduces non-linear behavior prior to 1,500 m/s.

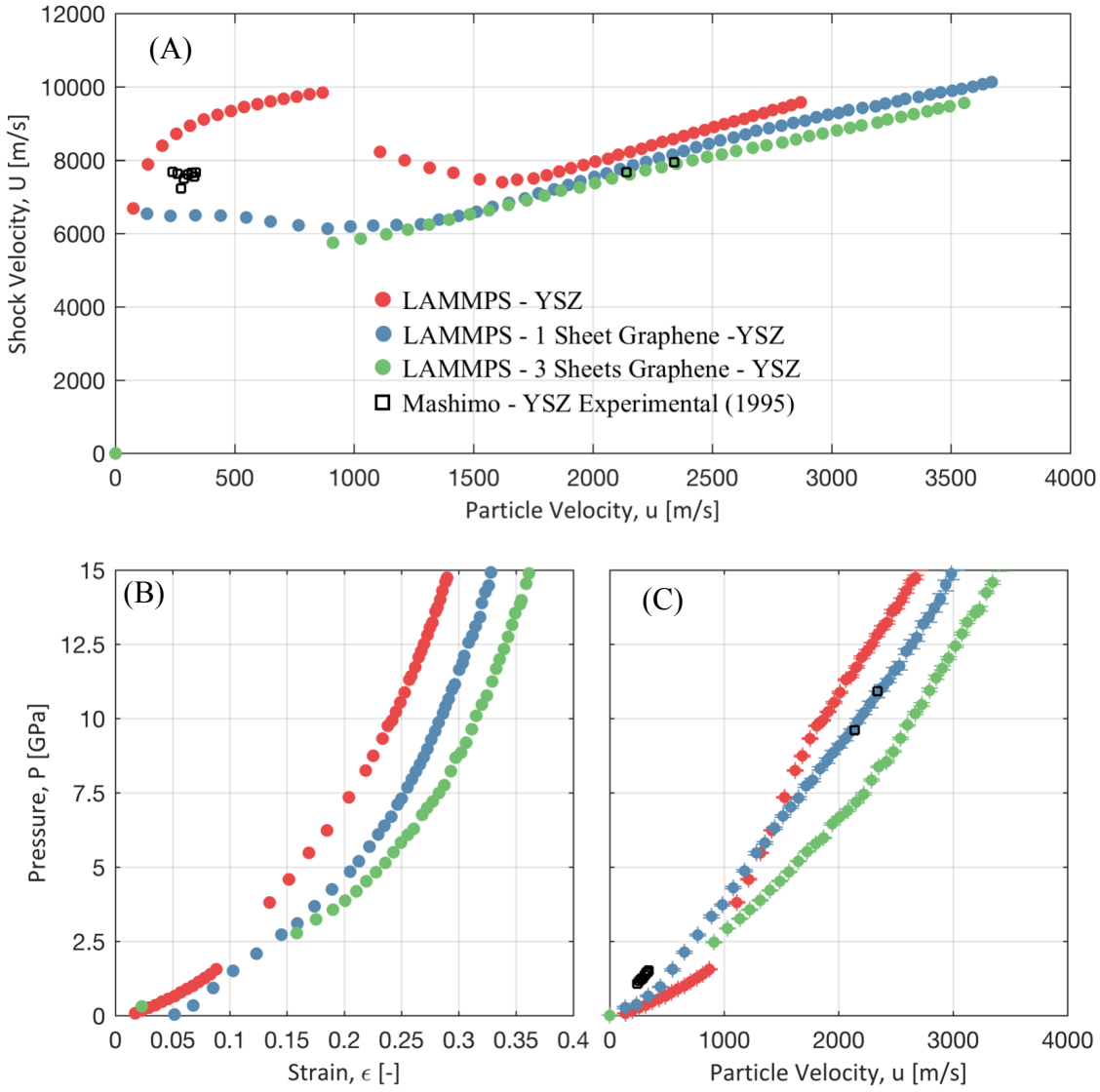

Figure 5.4: MD Hugoniot results (A) shock and particle velocity ($U-u$), (B) the pressure-strain ($P-\epsilon$), and (C) the pressure-particle velocity relationship ($P-u$).

Focusing on $P-\epsilon$ and $P-u$ relations illustrated in Figure 5.4B and 5.4C, observations can be made regarding the thermo-mechanical effects of shock compression. Comparison of the data in $P-\epsilon$ space shows that increasing graphene content increases strain exhibited by the ensemble. Results suggests that the compressibility between the graphene lattice and YSZ lattice is greater than what is exhibited by solely by the YSZ

lattice. This is not surprising considering the prescribed interatomic forces between the graphene and YSZ lattices are lesser in magnitude than the forces exhibited in the lattice. Next, consider results exhibited in the $P - u$ plane. Note the inverted relationship around a particle velocity of 1,000 m/s for the YSZ ensemble. For a given particle velocity less than 1,000 m/s, higher magnitudes of pressure are exhibited by ensembles with increased graphene. The relationship is then inverted for particle velocities greater than 1,000 m/s, and higher magnitudes of pressure are exhibited by ensembles with decreased graphene. This dynamic behavior may indicate that there is an impedance shift in the medium, aligning with Mashimo's previous statements.

Overall, results from the three thermo-mechanical planes suggest graphene does alter the dynamic response of the medium, based on the computationally implemented theory. It is believed that density and impedance differences between YSZ and graphene may greatly attribute to the phenomena observed. With this stated, the significance of the MD results provide the shock response of an idealized non-porous media composed of graphene and YSZ, and as such provides a benchmark for comparison with experimental data. In Section 5.3, further conversation on the MD results will be discussed, as the MD solutions will be directly compared to experimental results.

5.2 Experimental Test Series

A series of ten compaction experiments were performed on the YSZ variants discussed in Section 4.2.3. Eight of the ten targets remained affixed throughout the shot, and thus 32 sample materials were recovered for post-shot analysis. Targets were shot at projectile velocities ranging between 315 m/s and 586 m/s, imparting kinetic energies

between roughly 29 kJ and 100 kJ (projectile mass ~0.29 kg) into the target. It was observed that the fasteners used in the target yielded at velocities greater than 400 m/s, and samples were not recoverable (Targets 6 &7). To remedy this for impact velocities greater than 400 m/s, the interface between the driver and the anvil was welded together, and a soft recovery system was constructed using aluminum foam, aluminum honeycomb, and rubber mats. With this approach, samples were recovered at projectile velocities up to the aforementioned 586 m/s. An image of a recovered target and projectile have been included in Figure 5.5. Note the deformation seen in the steel target and the polycarbonate projectile.

Pertinent data, such as projectile, target, and sample measurements, can be found in Appendix A-Table 6.1 and Appendix A-Table 6.2. With use of these values, calculations for the Hugoniot parameters were performed by impedance matching the initial density of each sample with an associated projectile velocity and shock velocity. Illustrations of the $U - u$ and $P - \epsilon$ planes for each sample variation can be found in Figure 5.6, where impedance matching using the calculated Hugoniot relations satisfy the particle velocities observed in the reduced PDV traces from the sample/PMMA interface (Figure 5.7). Linear regressions were then fit to the locus of points for the samples in the $U - u$ planes (Table 5.1), and were used to calculate the trend lines found in the $P - \epsilon$ planes.

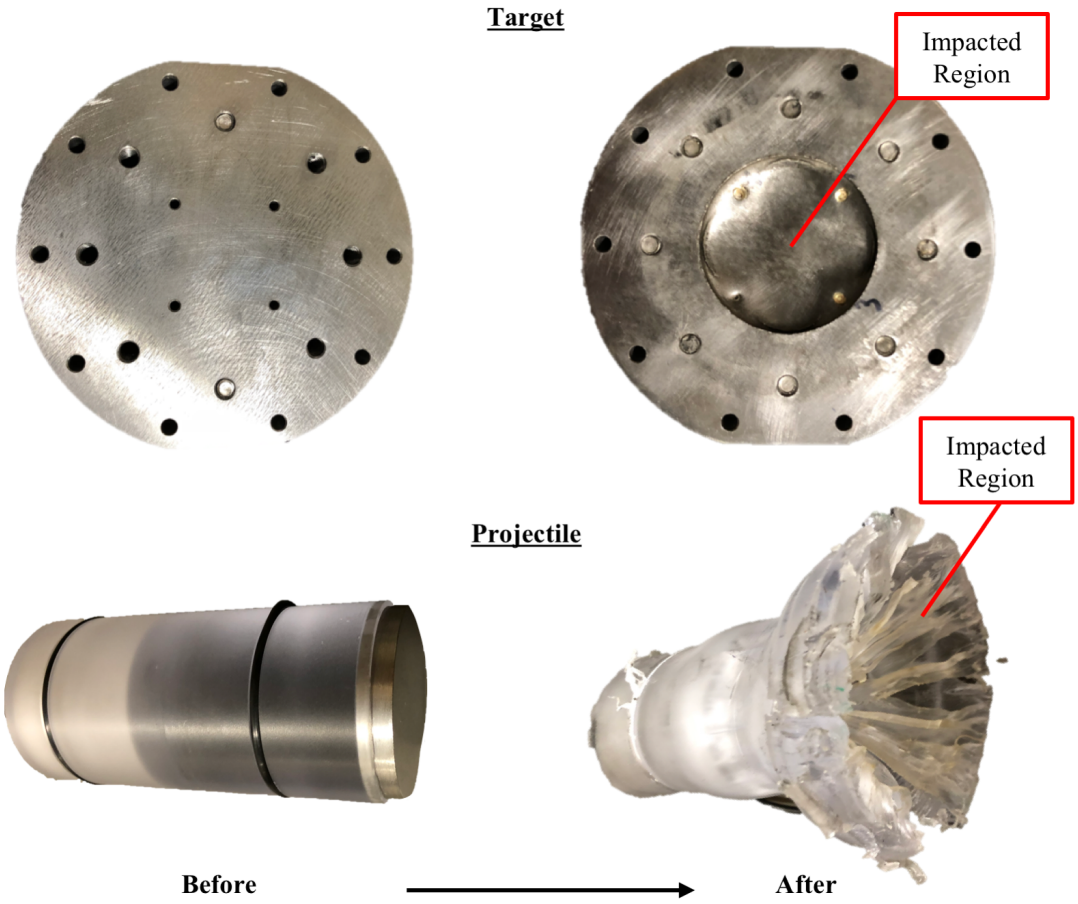

Figure 5.5: Photographs of the target and projectile before and after the experiment. Deformation can be noticed for the target and projectile in the impacted areas.

Table 5.1: Summary of the $U - u$ Hugoniot parameters for the powdered mixtures.

Material	Micro YSZ			Nano YSZ		
	$\rho_{00}\ (g/cc)$	$C_0(km/s)$	s	$\rho_{00}(g/cc)$	$C_0(km/s)$	s
0% wt. Graphene	2.820	0.626	1.31	2.402	0.538	1.40
1% wt. Graphene	3.282	0.558	1.99	2.899	0.336	2.42
3% wt. Graphene	3.362	0.834	1.33	2.978	0.499	1.90
5% wt. Graphene	3.405	0.831	1.38	2.850	0.381	2.29

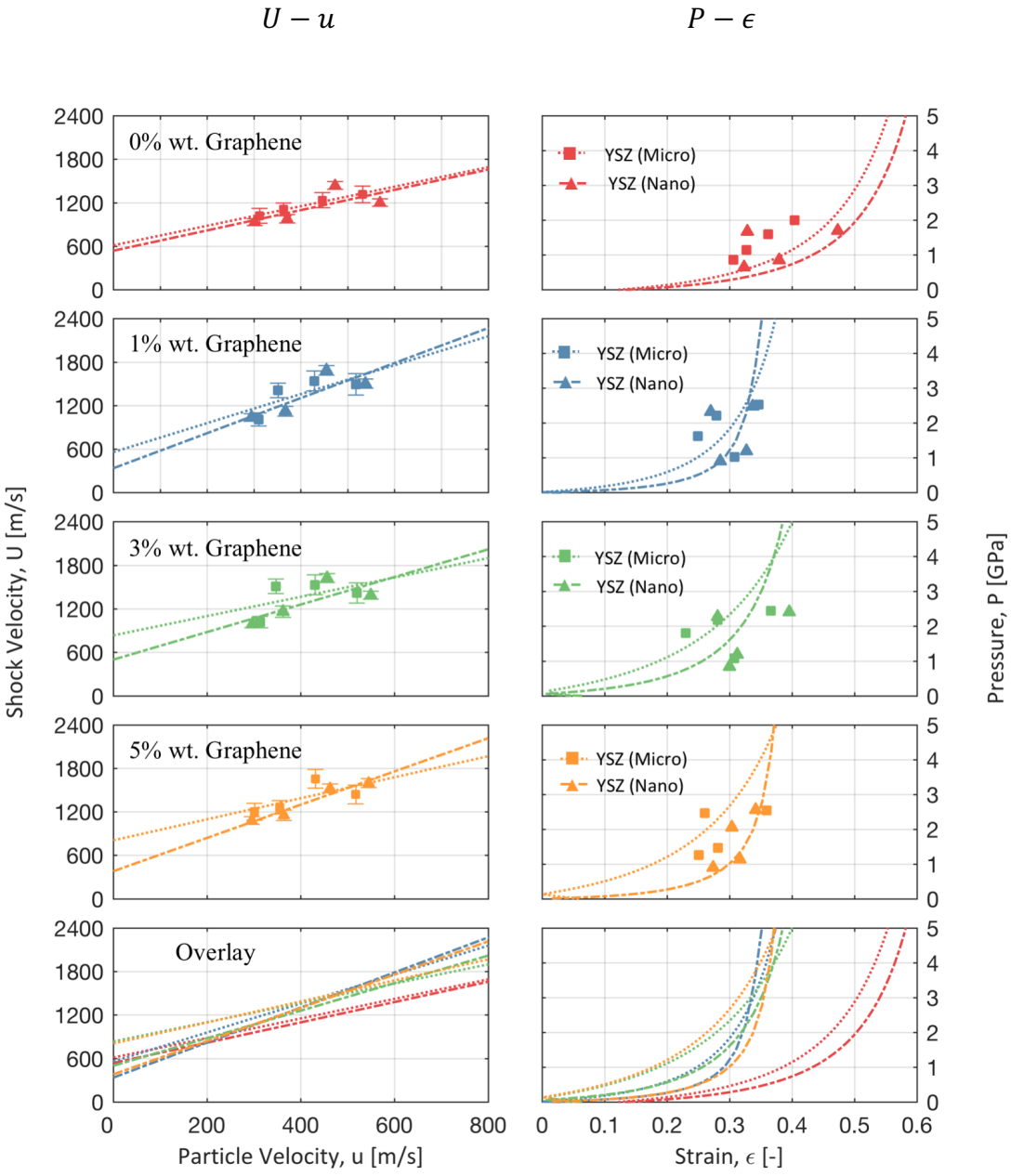

Figure 5.6: Comparison of the Hugoniot data for each particle size and weight percentage of graphene. Figures on the left depict the $U - u$ relationship, while figures on the right depict the $P - \epsilon$ relationship. From top to bottom, figures increase in graphene weight percentage. A direct comparison between the eight samples can be seen in the bottom row, where hashed and dotted lines depict the various nanometer and micrometer grain sizes, respectively.

The results presented in the $U - u$ and $P - \epsilon$ planes depict the shock response of the eight YSZ variants. In Figure 5.6, the influence of morphology can be observed between the micrometer and nanometer YSZ. A general trend can be noticed between the two particle sizes, such that the nanometer particle samples have slightly lower shock velocities relative to the micrometer particle size (Figure 5.6). Additionally, observation of the eight materials support that shock velocity would increase as the weight percentage of graphene was increased, however, samples composed of 1% weight graphene appear to achieve the highest shock velocities of the samples.

Figure 5.6 also illustrates an interesting story regarding the $P - \epsilon$ plane. Results indicate that higher magnitudes of strain were observed for the nanometer-YSZ under similar pressures when compared to the micrometer-YSZ samples. Results of such are suggestive that the lower initial density observed in the nanometer samples allowed for more void collapse in the media, allowing for higher compressibility to be achieved by the nanometer samples. For nanometer-YSZ samples, as the weight percentage of graphene was increased, similar strains corresponded to higher pressures. The micrometer-YSZ samples, however, observed the opposite trend. As the graphene weight percentage was increased, less strain was observed in the samples under similar loading conditions. Investigation of the initial density indicates the initial packing states likely were a substantial factor in this behavior, and that length scale differences between the graphene and YSZ particles attributed to the different packing densities.

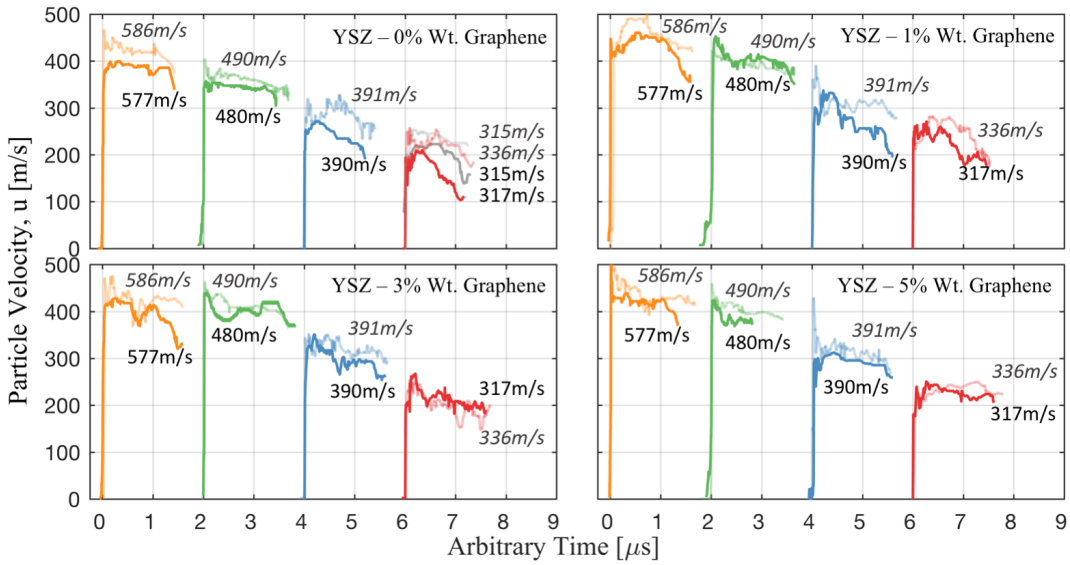

Figure 5.7: Particle velocity traces observed from the sample/PMMA interface. Plots are grouped by weight percentage of graphene, and colored by experiment (i.e. similar loading conditions). Bolded colors indicate nanometer YSZ, while lighter colors indicate micrometer YSZ.

It is important to note that the thermo-mechanical relations found in Figure 5.6 are impedance matched using particle velocities observed in the PDV traces of Figure 5.7. All traces have been plotted corresponding to material composition and particle size. Bolded traces correspond to nanometer particle size YSZ, while more transparent colors correspond to micrometer particle size. Coloration of the traces also correspond to the four samples impacted in an experiment. With these traces, observations can be made regarding the states of the material. It was observed that micrometer particle sizes typically observed higher particle velocities than their nanometer counterpart. In addition to this behavior, some observations can be made regarding the state achieved in the material. Most particle velocities appeared to remain constant, indicating that a Hugoniot state was held. Some variability may be exhibited in these states due to the heterogeneity and void collapse of the media. A few signals, exhibit slight dips in the particle velocities. This may be suggestive of fracture exhibited during compaction.

5.3 Porous comparison

The previous two sections outlined the results of molecular dynamics simulations and experimental data investigated. Comparison between the data sets provide understanding regarding the implications of porosity and heterogeneity in the samples.

Figure 5.8 and Figure 5.9 depict the $U - u$ and $P - \epsilon$ relations for the molecular dynamic and experimental results. The influence of porosity is easily illustrated between the MD simulations and experimental data in the $U - u$ plane. At comparable particle velocities, MD results have a much larger magnitude of shock velocity than experimental data. This can be attributed to porosity and heterogeneity being negated in the MD simulations. Factors such as heterogeneity and porosity are highly prevalent in the experimental samples, and appear to be a dominating factor in the reduced shock velocity in the media. A quantitative comparison reveals that the MD simulations obtain shock velocities spanning 5,500 m/s to 10,000 m/s, where shock velocities in the experimental data span between 800 m/s to 1,700 m/s. The difference in magnitude of shock velocity is apparent.

An additional remark can be made about the influences of graphene content. MD simulations indicate that increasing graphene content with no porosity decreases shock velocity. Experimental data of the porous media indicates an overall increase in shock velocity as the weight percentage of graphene is increased. Results of such demonstrate factors such as porosity and heterogeneity can invert the overall behavior of the media, ultimately changing the response of the medium.

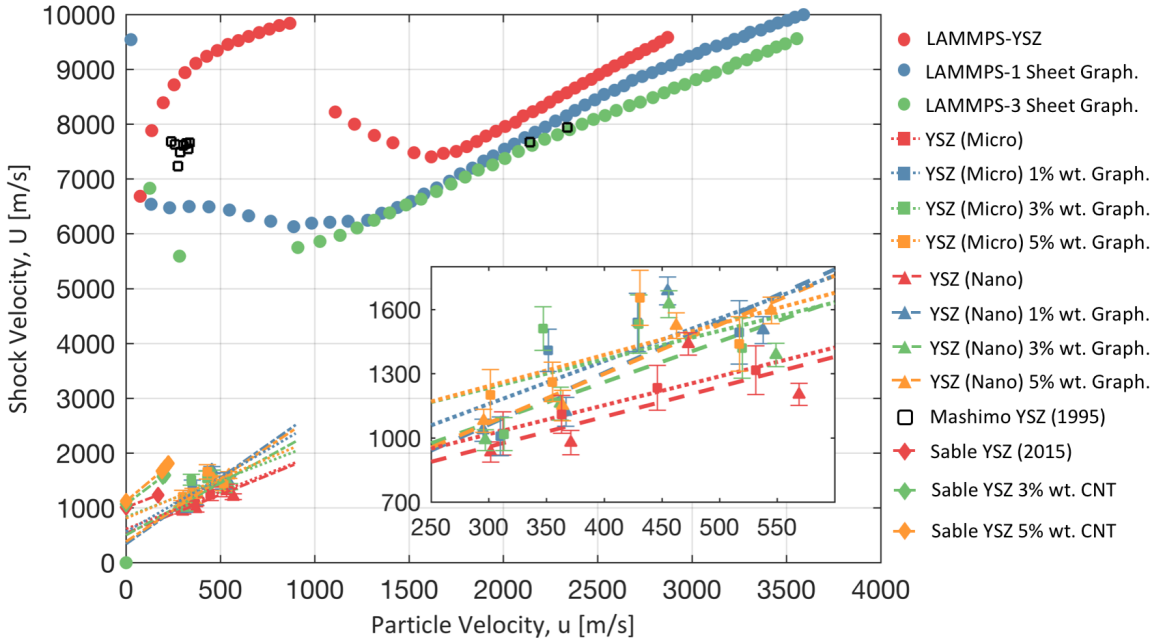

Figure 5.8: Hugoniot relations for the $U - u$ of the YSZ variants. Various colors are indicative of the weight percentage of graphene. Markers denote LAMMPS simulations, experimental data reported by Mashimo and Sable, and as the nanometer and micrometer YSZ grain sizes investigated.

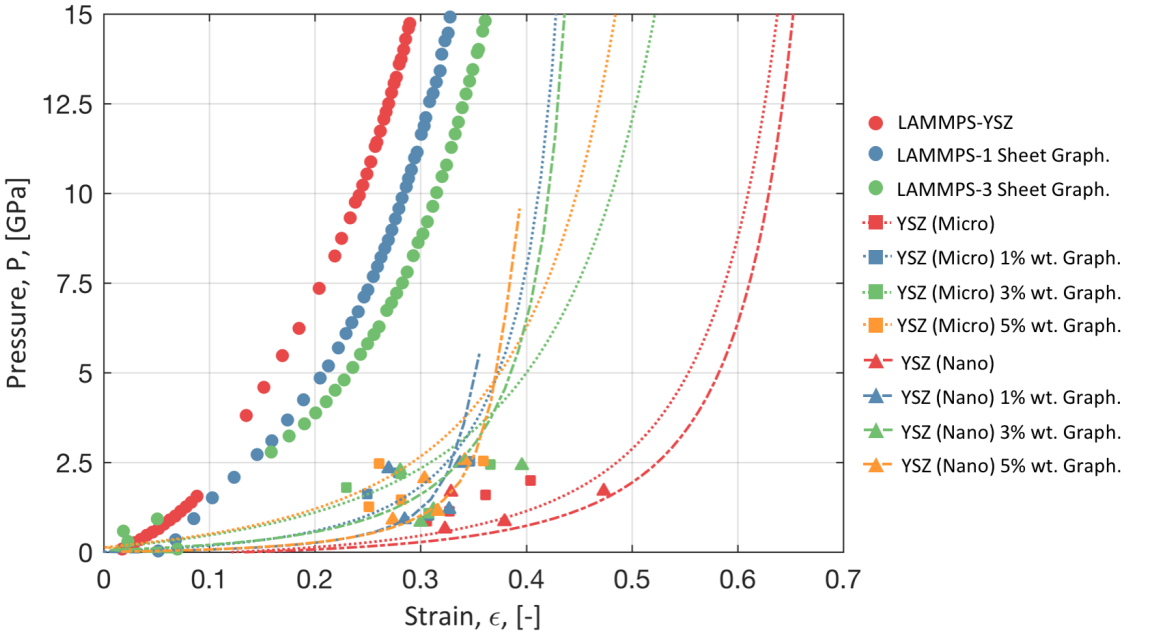

Figure 5.9: Relations for the $P - \epsilon$ of the YSZ variants. Colors indicative of the weight percentage of graphene. Markers denote LAMMPS simulations, as well as the nanometer and micrometer YSZ grain sizes investigated.

Comparison of the $P - \epsilon$ space illustrates the nature of the compaction states and overall compressibility of each specimen, with Figure 5.9 showing both MD results and experimental data. It can be noticed that strains observed in the MD simulations are much lower than those found in experiment. Recall that porosity is not exhibited in the MD simulations, strain is therefore solely compression of the lattice structures which is expected to have a much more stiff response. Experiments compressed the porous samples, collapsing voids and causing plastic deformation to the particles and lattices. Therefore, much higher magnitudes of strain were exhibited by the experimental samples relative to the MD simulations. It can be noticed that in the MD simulations that as the graphene content is increased, the strain increases at a similar pressure. The opposite is generally observed for the experimental data, where at a given pressure the strain is decreased as the graphene content is increased. This is the influence the packing of the particulate can have on dynamic behavior of the media.

6 DISCUSSION, CONCLUSION, AND FUTURE WORK

This work aimed to characterize graphene and YSZ materials far from thermodynamic equilibrium states. Characterization in this domain may allow for unique materials with desirable and tailorable material properties to be achieved. As part of characterization, thermo-mechanical mapping of graphene and YSZ mixtures were performed computationally and experimentally. Information collected in this work may be used to fabricate bulk YSZ and graphene composites to specific standards, allowing for more prevalent use in a variety of engineering applications.

Molecular dynamics simulations and experimental studies were conducted to study the dynamic compaction of graphene and YSZ mixtures, where underlying differences between the MD simulations and experimental studies exist in the porosity and heterogeneity of the media. The MD simulations illustrate non-porous dynamic behavior of the ensembles, while experiments depict influences of porosity and heterogeneity on the dynamic behavior of the materials.

In the MD studies, thermo-mechanical states were mapped using three different graphene and YSZ compositions. Experiments similarly mapped the thermo-mechanical states using various graphene and YSZ compositions. Findings identified that in non-porous media studied in the MD simulations, increasing graphene content reduced the density and impedance of the medium and resulted in higher strain. Experiments illustrated the opposite effect generally, where increasing graphene increased the packed density of the samples and reduced strain. Existing literature appears to match general trends observed for both data sets. Data published by Mashimo on the dynamic behavior of cubic YSZ appears to match the MD simulation results, and work published by Sable

on the dynamic compaction of carbon nanotube (CNT) and YSZ mixtures appears to exhibit similar trends to the experimental data of this work.

Further findings illustrate implications of heterogeneous structures in the packed graphene and YSZ samples. Recall that two YSZ particulate sizes were tested. It was found that the initial packing state of the micro-YSZ samples achieved higher density magnitudes relative to the nano-YSZ, and density increased for both particle sizes as the graphene weight percentage was increased. This suggests that length scale differences or shape factors between micro-YSZ particle and graphene may allow for graphene to decrease porosity in the packed state of the media. This effect appeared to increase the shock velocity of the samples, as well as reduced strain. It is important to note, however, that reducing porosity in samples may increase inter-particulate friction and affect the consolidation of particles in the samples. Fracture toughness of the compacted samples may vary depending on the compacted specimen's porosity.

An additional comment can be made regarding the compaction state of the samples. With the consolidation criterion set forth by Schwarz et al., pressure and time duration of the loading state can be inferred from the PDV traces presented in Figure 5.7. Results indicate that the samples were subjected to a loading states of two microseconds, however, pressures below 3 GPa were recorded. This information therefore suggests that inter-particulate bonding was likely not achieved in the samples. Samples likely are highly densified and exhibit rigidity with no inter-particulate bonding. For discussion, SEM images of the micrometer grain YSZ variants were included in Appendix C - Figure 6.1, and the images appear to depict that the samples have been compacted. It is difficult, however, to make conclusive statements regarding the status of the consolidation. Post-

shot analysis regarding the consolidated nature will be performed by Oceanit. Although the samples may not be fully consolidated, the mapped thermo-mechanical state allows for extrapolation of the data, and should allow for calculations to be performed to achieve a fully consolidated state.

Between the MD simulations and experimental data, limitations exist regarding conclusive statements that can be made regarding the phase and thermodynamic space of the various materials. The MD simulations inform on dynamic behavior of the medium, however, conclusive statements cannot be made regarding potential phase change of the YSZ. Results are suggestive that a phase change may occur, however, further study regarding the free energy of the atomic ensembles could provide telling information. Attempts at determining the phase change in the YSZ were performed, however, proved unsuccessful. Studies were attempted in LAMMPS using the Free Energy Perturbation (FEP) technique, and proved unsuccessful.

Drawing attention to the experimental data, ten experimental series were performed. These studies allowed for four states to be observed per composition type. Further experimental mapping of the thermo-mechanical states may provide extended accuracy regarding the modeling of the non-equilibrium behavior of the compositions. In a positive light, the models developed in this work can be extrapolated to predict further behavior of the medium.

The results exhibited experimentally were governed by the packed nature of the samples. Recall that samples were packed by pressing all the samples to a uniform pressure. Although consistency was implemented by pressing the samples to uniform pressures, the density states varied slightly depending on composition. To isolate

implications of graphene in a different respect, uniform densities may provide a different insight into the shock response of the media. Studying material compositions with this regard may yield similar trends to the MD results.

With these limiting statements made for the MD simulations and experiments, future works could further characterize material properties of graphene and YSZ composites. Free energy calculations could be used to characterize phase shifts in the lattice of YSZ. Additional experimental studies could continue to map the thermo-mechanical states of the materials. Lastly, packing the loose powders using a different method may shed light on the material dynamics from a different respect.

In closing, this study provided thermo-mechanical modeling of graphene and YSZ compositions using MD simulations and gas-gun experiments. Results illustrate the significant implications that porosity and heterogeneity can have on the compaction dynamics. Because samples were recovered from the experiments, property characterization allows for fabrication to be tailored to the desire of the manufacturer. With the thermo-mechanical models found in the work, manufacturing techniques can be designed to satisfy the thermodynamic conditions necessary to manufacture desired graphene and YSZ composites for use in engineering applications.

BIBLIOGRAPHY

[1] G. Stapper, M. Bernasconi, N. Nicoloso, and M. Parrinello, “Ab initio study of structural and electronic properties of yttria-stabilized cubic zirconia,” *Phys. Rev. B*, vol. 59, no. 2, pp. 797–810, 1999.

[2] W. J. Fleming, “Physical Principles Governing Nonideal Behavior of the Zirconia Oxygen Sensor,” *J. Electrochem. Soc.*, vol. 124, no. 1, p. 21, 1977.

[3] M. A. Parkes, “ab initio Modeling of Yttria Stabilised Zirconia for Solid Oxide Fuel Cells,” Imperial College London, 2015.

[4] S. Badwal, “Zirconia-based solid electrolytes: microstructure, stability and ionic conductivity,” *Solid State Ionics*, vol. 52, no. 1–3, pp. 23–32, May 1992.

[5] C. Piconi and G. Maccauro, “Zirconia as a ceramic biomaterial,” *Biomaterials*, vol. 20, no. 1, pp. 1–25, 1999.

[6] A. Gallardo-lópez, I. Márquez-abril, A. Morales-rodríguez, and A. Muñoz, “Dense graphene nanoplatelet / yttria tetragonal zirconia composites : Processing , hardness and electrical conductivity,” *Ceram. Int.*, vol. 43, no. 15, pp. 11743–11752, 2017.

[7] J. H. Shin and S. H. Hong, “Fabrication and properties of reduced graphene oxide reinforced yttria-stabilized zirconia composite ceramics,” *J. Eur. Ceram. Soc.*, vol. 34, no. 5, pp. 1297–1302, 2014.

[8] M. Mazaheri, D. Mari, R. Schaller, G. Bonnefont, and G. Fantozzi, “Processing of yttria stabilized zirconia reinforced with multi-walled carbon nanotubes with attractive mechanical properties,” *J. Eur. Ceram. Soc.*, vol. 31, no. 14, pp. 2691–2698, 2011.

[9] K. C. Lau and B. I. Dunlap, “Molecular dynamics simulation of yttria-stabilized zirconia (YSZ) crystalline and amorphous solids,” *J. Phys. Condens. Matter*, vol. 23, no. 3, 2011.

[10] X. Xia, “Computational Modelling Study of Yttria-stabilized Zirconia Thesis submitted for the degree of Doctor of Philosophy Xin Xia,” *Ph.D thesis*, 2010.

[11] X. Z. Wang, X. Y. Liu, A. Javed, C. Zhu, and G. Y. Liang, “Phase transition behavior of yttria-stabilized zirconia from tetragonal to monoclinic in the lanthanum zirconate/yttria-stabilized zirconia coupled-system using molecular

dynamics simulation," *J. Mol. Liq.*, vol. 207, pp. 309–314, 2015.

[12] J. Hu, X. Ruan, and Y. P. Chen, "Thermal conductivity and thermal rectification in graphene nanoribbons: a molecular dynamics study.," *Nano Lett.*, vol. 9, no. 7, p. 2730, 2009.

[13] J. W. Jiang, J. S. Wang, and B. Li, "Young's modulus of graphene: A molecular dynamics study," *Phys. Rev. B - Condens. Matter Mater. Phys.*, vol. 80, no. 11, pp. 15–18, 2009.

[14] A. Bagri, S. P. Kim, R. S. Ruoff, and V. B. Shenoy, "Thermal transport across twin grain boundaries in polycrystalline graphene from nonequilibrium molecular dynamics simulations," *Nano Lett.*, vol. 11, no. 9, pp. 3917–3921, 2011.

[15] T. Mashimo, A. Nakamura, M. Kodama, K. Kusaba, K. Fukuoka, and Y. Syono, "Yielding and Phase-Transition Under Shock Compression of Yttria-Doped Cubic Zirconia Single-Crystal and Polycrystal," *J. Appl. Phys.*, vol. 77, no. 10, pp. 5060–5068, 1995.

[16] P. A. Sable, J. LaJeunesse, C. Sullivan, V. Kamavaram, and J. P. Borg, "Dynamic compaction of yttria-stabilized zirconia with the addition of carbon-nanotubes," in *AIP Conference Proceedings*, 2017, p. 120004.

[17] K. Hokamoto, S. Tanaka, M. Fujita, S. Itoh, M. A. Meyers, and H. C. Chen, "High temperature shock consolidation of hard ceramic powders," *Phys. B Condens. Matter*, vol. 239, no. 1–2, pp. 1–5, 1997.

[18] Q. Zhou, P. W. Chen, X. Gao, and W. P. Shen, "Experiment Study on the Hot-Shock Consolidation of Tungsten Powder," *Mater. Sci. Forum*, vol. 673, pp. 107–112, 2011.

[19] J. Beck, M. Alvarado, D. Nemir, M. Nowell, L. Murr, and N. Prasad, "Shock-wave consolidation of nanostructured bismuth telluride powders," *J. Electron. Mater.*, vol. 41, no. 6, pp. 1595–1600, 2012.

[20] P. Peyre and R. Fabbro, "Laser Shock Processing: A Review of the Physics and Applications," *Opt. Quantum Electron.*, vol. 27, pp. 1213–1229, 1995.

[21] C. Deng, M. Liu, and P. Molian, "Nanodiamond powder compaction via laser shockwaves: Experiments and finite element analysis," *Powder Technol.*, vol. 239, pp. 36–46, 2013.

[22] D. H. Ahn, W. Kim, M. Kang, L. J. Park, S. Lee, and H. S. Kim, "Plastic

deformation and microstructural evolution during the shock consolidation of ultrafine copper powders," *Mater. Sci. Eng. A*, vol. 625, pp. 230–244, 2015.

[23] P. Kasiraj, T. Vreeland, R. B. Schwarz, and T. J. Ahrens, "Shock consolidation of a rapidly solidified steel powder," *Acta Metallurgica*, vol. 32, no. 8. pp. 1235–1241, 1984.

[24] D. A. Fredenburg, D. Dennis-Koller, and D. M. Dattelbaum, "Shock consolidation response of CeO 2 powders," *AIP Conf. Proc.*, vol. 1426, pp. 1487–1490, 2012.

[25] W. Tong, G. Ravichandran, T. Christman, and T. Vreeland, "Processing SiC-particulate reinforced titanium-based metal matrix composites by shock wave consolidation," *Acta Metall. Mater.*, vol. 43, no. 1, pp. 235–250, 1995.

[26] M. A. Meyers, *Dynamic behavior of materials.* New York : Wiley, c1994., 1994.

[27] R. B. Schwarz, P. Kasiraj, T. J. Vreeland, and T. J. Ahrens, "A Theory for the Shock-Wave Consolidation of Powders," *Acta Mater.*, vol. 32, pp. 1243–1252, 1984.

[28] T. J. Ahrens *et al.*, "Shock Consolidation of Aluminum-Lithium Powder," New York: Marcel Dekker Inc, 1986, pp. 83–106.

[29] T. Akashi, V. Lotrich, A. Sawaoka, and E. K. Beauchamp, "Shock Consolidation of Coarse Sic Powder," *J. Am. Ceram. Soc.*, vol. 68, no. 12, p. C-322-C-324, 1985.

[30] F. D. S. Marquis, A. Mahajan, and A. G. Mamalis, "Shock synthesis and densification of tungsten based heavy alloys," vol. 161, pp. 113–120, 2005.

[31] G. Sh, A. S. Kaygorodov, and N. B. Volkov, "Densification of the granular medium by the low amplitude shock waves," vol. 234, pp. 223–234, 2009.

[32] D. A. Fredenburg and N. N. Thadhani, "On predicting the shock densification response of heterogeneous powder mixtures," *AIP Conf. Proc.*, vol. 1426, pp. 1479–1482, 2012.

[33] J. P. Borg and T. J. Vogler, "Rapid compaction of granular material: Characterizing two- and three-dimensional mesoscale simulations," *Shock Waves*, vol. 23, no. 2, pp. 153–176, 2013.

[34] M. A. Meyers, D. J. Benson, and E. A. Olevsky, "Shock consolidation: microstructurally-based analysis and computational modeling," *Acta Mater.*, vol. 47, no. 7, pp. 2089–2108, 1999.

[35] J. M. D. Lane, A. P. Thompson, and T. J. Vogler, “Enhanced densification under shock compression in porous silicon,” *Phys. Rev. B - Condens. Matter Mater. Phys.*, vol. 90, no. 13, pp. 1–6, 2014.

[36] G. Fenton, D. Grady, and T. Vogler, “Intense shock compression of porous solids: Application to WC and Ta 2O 5,” in *AIP Conference Proceedings*, 2012, vol. 1426, no. 2012, pp. 1463–1466.

[37] F. M. White, *Fluid Mechanics*. McGraw-Hill, 2008.

[38] P. W. Cooper, *Explosives engineering*. New York, N.Y. : Wiley-VCH, c1996., 1996.

[39] Y. A. Çengel and M. A. Boles, *Thermodynamics : an engineering approach*. 2015.

[40] “LAMMPS Molecular Dynamics Simulator.” Sandia National Laboratories, Albuquerque, New Mexico, 2017.

[41] S. Plimpton, “Fast Parallel Algorithms for Short – Range Molecular Dynamics,” *J. Comput. Phys.*, vol. 117, no. June 1994, pp. 1–19, 1995.

[42] J. Li, “AtomEye: An efficient atomistic configuration viewer,” *Model. Simul. Mater. Sci. Eng.*, vol. 11, no. 2, pp. 173–177, 2003.

[43] W. Humphrey, A. Dalke, and K. Schulten, “{VMD} -- {V}isual {M}olecular {D}ynamics,” *J. Mol. Graph.*, vol. 14, pp. 33–38, 1996.

[44] J. Eargle, D. Wright, and Z. Luthey-Schulten, “Multiple Alignment of protein structures and sequences for VMD,” *Bioinformatics*, vol. 22, no. 4, pp. 504–506, Feb. 2006.

[45] J. Stone, J. Gullingsrud, P. Grayson, and K. Schulten, “A System for Interactive Molecular Dynamics Simulation,” in *2001 ACM Symposium on Interactive 3D Graphics*, 2001, pp. 191–194.

[46] J. Stone, “\em An Efficient Library for Parallel Ray Tracing and Animation,” Computer Science Department, University of Missouri-Rolla, 1998.

[47] D. Frishman and P. Argos, “Knowledge-based secondary structure assignment,” *Proteins Struct. Funct. Genet.*, vol. 23, pp. 566–579, 1995.

[48] A. Varshney, F. P. Brooks, and W. V Wright, “Linearly Scalable Computation of Smooth Molecular Surfaces,” *IEEE Comput. Graph. Appl.*, vol. 14, pp. 19–25,

1994.

[49] M. Sanner, A. Olsen, and J.-C. Spehner, “Fast and Robust Computation of Molecular Surfaces,” in *Proceedings of the 11th ACM Symposium on Computational Geometry*, 1995, pp. C6–C7.

[50] A. Stukowski, “Modelling and Simulation in Materials Science and Engineering Visualization and analysis of atomistic simulation data with OVITO – the Open Visualization Tool Visualization and analysis of atomistic simulation data with OVITO – the Open Visualization Tool,” 2010.

[51] D. Reddy, L. F. Register, G. D. Carpenter, and S. K. Banerjee, “Graphene field-effect transistors,” *Journal of Physics D: Applied Physics*, vol. 44, no. 31. 2011.

[52] P. K. Schelling, S. R. Phillpot, and D. Wolf, “Mechanism of the Cubic-to-Tetragonal Phase Transition in Zirconia and Yttria-Stabilized Zirconia by Molecular-Dynamics Simulation,” *J. Am. Ceram. Soc.*, vol. 84, no. 7, pp. 1609–1619, 2004.

[53] J. P. Bouanich, “Site-site Lennard-Jones potential parameters for N2, O2, H2, CO and CO2,” *J. Quant. Spectrosc. Radiat. Transf.*, vol. 47, no. 4, pp. 243–250, 1992.

[54] M. Kaukonen, A. Gulans, P. Havu, and E. Kauppinen, “Lennard-Jones parameters for small diameter carbon nanotubes and water for molecular mechanics simulations from van der Waals density functional calculations,” *J. Comput. Chem.*, vol. 33, no. 6, pp. 652–658, 2012.

[55] B. Suo and K. Balasubramanian, “Spectroscopic constants and potential energy curves of yttrium carbide (YC),” *J. Chem. Phys.*, vol. 126, no. 22, 2007.

[56] M. Prakash *et al.*, “Diffusion of H2, CO2, and Their Mixtures in the Porous Zirconium Based Metal-Organic Framework MIL-140A(Zr): Combination of Quasi-Elastic Neutron Scattering Measurements and Molecular Dynamics Simulations,” *J. Phys. Chem. C*, vol. 119, no. 42, pp. 23978–23989, 2015.

[57] R. Ravelo, B. L. Holian, T. C. Germann, and P. S. Lomdahl, “Constant-stress Hugoniostat method for following the dynamical evolution of shocked matter,” *Phys. Rev. B - Condens. Matter Mater. Phys.*, vol. 70, no. 1, pp. 1–9, 2004.

[58] J. R. Asay and M. Shahinpoor, *High pressure shock compression of solids.* New York, USA : Springer, 1993., 1992.

[59] G. T. Gray, “Influence of Shock-Wave Deformation on the Structure/Property

Behavior of Materials BT - High-Pressure Shock Compression of Solids," J. R. Asay and M. Shahinpoor, Eds. New York, NY: Springer New York, 1993, pp. 187–215.

[60] S. Chantrenne, J. L. Wise, J. R. Asay, M. E. Kipp, and C. A. Hall, "Design of a sample recovery assembly for magnetic ramp-wave loading," *AIP Conf. Proc.*, vol. 1195, pp. 695–698, 2009.

[61] D. A. Crawford, "CTH User's Manual and Input Instructions." Sandia National Laboratories, Albuquerque, New Mexico, 2017.

[62] N. S. Helminiak, "Construction and Characterization of a Single Stage Dual Diaphragm Gas Gun," 2017.

[63] D. H. Dolan, M. Elert, M. D. Furnish, W. W. Anderson, W. G. Proud, and W. T. Butler, "WHAT DOES 'VELOCITY' INTERFEROMETRY REALLY MEASURE?," in *AIP Conference Proceedings*, 2009, pp. 589–594.

[64] D. H. Dolan, "Accuracy and precision in photonic doppler velocimetry," *Rev. Sci. Instrum.*, vol. 81, no. 5, 2010.

[65] B. J. Jensen, D. B. Holtkamp, P. A. Rigg, and D. H. Dolan, "Accuracy limits and window corrections for photon Doppler velocimetry," *J. Appl. Phys.*, vol. 101, no. 1, 2007.

[66] B. Zuanetti, T. Wang, and V. Prakash, "A compact fiber optics-based heterodyne combined normal and transverse displacement interferometer," *Rev. Sci. Instrum.*, vol. 88, no. 3, pp. 1–7, 2017.

[67] E. A. Moro and M. E. Briggs, "Note: Simultaneous measurement of transverse speed and axial velocity from a single optical beam," *Rev. Sci. Instrum.*, vol. 84, no. 1, 2013.

[68] G. Chen, D. Wang, J. Liu, J. Meng, S. Liu, and Q. Yang, "A novel photonic Doppler velocimetry for transverse velocity measurement," *Rev. Sci. Instrum.*, vol. 84, no. 1, 2013.

[69] T. D. Nichols, D. C. Harrison, and S. S. Alpert, "Simple laboratory demonstration of the Doppler shift of laser light," *Am. J. Phys.*, vol. 53, no. 7, pp. 657–660, 1985.

[70] O. T. Strand, D. R. Goosman, C. Martinez, T. L. Whitworth, and W. W. Kuhlow, "Compact system for high-speed velocimetry using heterodyne techniques," *Rev. Sci. Instrum.*, vol. 77, no. 8, pp. 1–8, 2006.

[71] O. T. Strand, L. V Berzins, D. R. Goosman, W. Kuhlow, P. D. Sargis, and T. L. Whitworth, “Velocimetry Using Heterodyne Techniques,” 2004.

[72] C. R. Johnson, J. W. Lajeunesse, P. A. Sable, A. Dawson, A. Hatzenbihler, and J. P. Borg, “Photon Doppler velocimetry measurements of transverse surface velocities,” *Rev. Sci. Instrum.*, vol. 89, no. 6, 2018.

[73] D. [Sandia N. L. Wackerbarth, “PlotData v. 4.47.” United States, 2016.

APPENDIX A – MEASUREMENTS

Table 6.1: Projectile and target measurements from each experiment.

Shot No.	*Projectile Mass (kg)*	*Projectile Velocity (km/s)*	*KE (kJ)*	*Target Thickness (mm)*	*Target Diameter (mm)*	*Target Weight (kg)*
1	0.2959 ± 0.0001	315 ± 12	29.360 ± 2.246	38.46 ± 0.01	113.69 ± 0.01	2.8854 ± 0.0001
2	0.2895 ± 0.0001	317 ± 12	29.091 ± 2.212	38.70 ± 0.01	113.84 ± 0.01	2.8799 ± 0.0001
3	0.2900 ± 0.0001	325 ± 12	30.602 ± 2.270	38.34 ± 0.01	113.56 ± 0.01	2.8752 ± 0.0001
4	0.2897 ± 0.0001	392 ± 15	44.516 ± 3.422	38.61 ± 0.01	113.70 ± 0.01	2.8818 ± 0.0001
5	0.2900 ± 0.0001	391 ± 15	44.335 ± 3.417	38.20 ± 0.01	114.25 ± 0.01	2.8509 ± 0.0001
6	0.2900 ± 0.0001	480 ± 19	66.816 ± 5.312	38.22 ± 0.01	114.25 ± 0.01	2.8488 ± 0.0001
7	0.2862 ± 0.0001	490 ± 19	68.716 ± 5.353	38.23 ± 0.01	114.22 ± 0.01	2.8507 ± 0.0001
8	0.2897 ± 0.0001	577 ± 23	96.449 ± 7.722	38.24 ± 0.01	114.26 ± 0.01	2.8470 ± 0.0001
9	0.2823 ± 0.0001	336 ± 13	31.866 ± 2.477	38.42 ± 0.01	114.25 ± 0.01	2.8556 ± 0.0001
10	0.2889 ± 0.0001	586 ± 24	99.207 ± 8.161	38.41 ± 0.01	114.24 ± 0.01	2.8602 ± 0.0001

Table 6.2: Sample measurements for each target.

Shot No.	*Sample No.*	*Sample*	*Particle Size* (m)	*Weight* (g)	*Volume* (cc)	*Density,* $\rho_{00}\ (g/cc)$	*Porosity*
$1^{+\circ}$	1	*NSDC	-	0.7914 ± 0.0001	0.39154 ± 0.01233	2.0212 ± 0.0637	0.65 ± 0.01
	2	*SDC	-	0.4374 ± 0.0001	0.31530 ± 0.00993	1.3872 ± 0.0437	0.42 ± 0.01
	3	YSZ	Nano	2.0839 ± 0.0001	0.86537 ± 0.02722	2.4081 ± 0.0758	0.59 ± 0.01
	4	YSZ	Micro	1.8168 ± 0.0001	0.61781 ± 0.01944	2.9407 ± 0.0925	0.50 ± 0.01
$2^{+\circ}$	5	YSZ	Nano	1.8991 ± 0.0001	0.82263 ± 0.02588	2.3086 ± 0.0726	0.61 ± 0.01
	6	1% wt. Gr. YSZ	Nano	1.8645 ± 0.0001	0.63102 ± 0.01986	2.9547 ± 0.0930	0.50 ± 0.01
	7	3% wt. Gr. YSZ	Nano	1.8685 ± 0.0001	0.65574 ± 0.02064	2.8495 ± 0.0897	0.52 ± 0.01
	8	5% wt. Gr. YSZ	Nano	1.8601 ± 0.0001	0.66065 ± 0.02079	2.8156 ± 0.0886	0.52 ± 0.01
3^{+}	9	YSZ	Micro	1.8345 ± 0.0001	0.69193 ± 0.02177	2.6513 ± 0.0834	0.55 ± 0.01
	10	1% wt. Gr. YSZ	Micro	1.8435 ± 0.0001	0.60012 ± 0.01889	3.0719 ± 0.0967	0.48 ± 0.01
	11	3% wt. Gr. YSZ	Micro	1.8210 ± 0.0001	0.58459 ± 0.01840	3.1150 ± 0.0980	0.47 ± 0.01
	12	5% wt. Gr. YSZ	Micro	1.8060 ± 0.0001	0.56244 ± 0.01770	3.2110 ± 0.1011	0.45 ± 0.01
$4^{+\circ}$	13	YSZ	Nano	1.8593 ± 0.0001	0.78940 ± 0.02484	2.3553 ± 0.0741	0.60 ± 0.01
	14	1% wt. Gr. YSZ	Nano	1.8921 ± 0.0001	0.65257 ± 0.02054	2.8995 ± 0.0912	0.51 ± 0.01
	15	3% wt. Gr. YSZ	Nano	1.8233 ± 0.0001	0.64501 ± 0.02030	2.8268 ± 0.0890	0.52 ± 0.01
	16	5% wt. Gr. YSZ	Nano	1.8133 ± 0.0001	0.66484 ± 0.02092	2.7274 ± 0.0858	0.54 ± 0.01
$5^{+\circ}$	17	YSZ	Micro	1.7444 ± 0.0001	0.61710 ± 0.01942	2.8268 ± 0.0890	0.52 ± 0.01
	18	1% wt. Gr. YSZ	Micro	1.7506 ± 0.0001	0.53333 ± 0.01679	3.2824 ± 0.0890	0.44 ± 0.01
	19	3% wt. Gr. YSZ	Micro	1.7700 ± 0.0001	0.51513 ± 0.01622	3.4360 ± 0.1033	0.42 ± 0.01
	20	5% wt. Gr. YSZ	Micro	1.7790 ± 0.0001	0.54415 ± 0.01713	3.2693 ± 0.1029	0.44 ± 0.01
6°	21	YSZ	Nano	1.7863 ± 0.0001	0.72695 ± 0.02287	2.4573 ± 0.0773	0.58 ± 0.01
	22	1% wt. Gr. YSZ	Nano	1.8159 ± 0.0001	0.59941 ± 0.01887	3.0295 ± 0.0954	0.49 ± 0.01
	23	3% wt. Gr. YSZ	Nano	1.7744 ± 0.0001	0.57860 ± 0.01821	3.0667 ± 0.0965	0.48 ± 0.01
	24	5% wt. Gr. YSZ	Nano	1.7479 ± 0.0001	0.59972 ± 0.01888	2.9145 ± 0.0917	0.51 ± 0.01
7°	25	YSZ	Micro	1.8000 ± 0.0001	0.62168 ± 0.01957	2.8954 ± 0.0911	0.51 ± 0.01
	26	1% wt. Gr. YSZ	Micro	1.7830 ± 0.0001	0.53170 ± 0.01674	3.3534 ± 0.1056	0.43 ± 0.01
	27	3% wt. Gr. YSZ	Micro	1.8142 ± 0.0001	0.54833 ± 0.01726	3.3086 ± 0.1042	0.44 ± 0.01
	28	5% wt. Gr. YSZ	Micro	1.8259 ± 0.0001	0.52811 ± 0.01663	3.4574 ± 0.1088	0.41 ± 0.01
$8^{+\circ}$	29	YSZ	Nano	1.8451 ± 0.0001	0.74191 ± 0.02334	2.4870 ± 0.0783	0.58 ± 0.01
	30	1% wt. Gr. YSZ	Nano	1.8462 ± 0.0001	0.58243 ± 0.01663	3.1698 ± 0.0998	0.46 ± 0.01
	31	3% wt. Gr. YSZ	Nano	1.8333 ± 0.0001	0.57875 ± 0.01822	3.1677 ± 0.0997	0.46 ± 0.01
	32	5% wt. Gr. YSZ	Nano	1.8113 ± 0.0001	0.61572 ± 0.01938	2.9418 ± 0.0926	0.50 ± 0.01
$9^{+\circ}$	33	YSZ	Micro	1.7641 ± 0.0001	0.65181 ± 0.02051	2.7064 ± 0.0852	0.54 ± 0.01
	34	1% wt. Gr. YSZ	Micro	1.7370 ± 0.0001	0.52835 ± 0.01663	3.2876 ± 0.1035	0.44 ± 0.01
	35	3% wt. Gr. YSZ	Micro	1.8578 ± 0.0001	0.54704 ± 0.01722	3.3961 ± 0.1069	0.42 ± 0.01
	36	5% wt. Gr. YSZ	Micro	1.8286 ± 0.0001	0.52548 ± 0.01654	3.4799 ± 0.1095	0.41 ± 0.01
$10^{+\circ}$	37	YSZ	Micro	1.8405 ± 0.0001	0.64536 ± 0.02031	2.8519 ± 0.0897	0.52 ± 0.01
	38	1% wt. Gr. YSZ	Micro	1.8303 ± 0.0001	0.55885 ± 0.01759	3.2751 ± 0.1031	0.44 ± 0.01
	39	3% wt. Gr. YSZ	Micro	1.8070 ± 0.0001	0.54604 ± 0.01719	3.3093 ± 0.1042	0.44 ± 0.01
	40	5% wt. Gr. YSZ	Micro	1.8273 ± 0.0001	0.53522 ± 0.01685	3.4141 ± 1075	0.42 ± 0.01

*Data not reported. $^{+}$Soft recovered target. $^{\circ}$ Data collected.

APPENDIX B – TARGET DESIGN

Target:

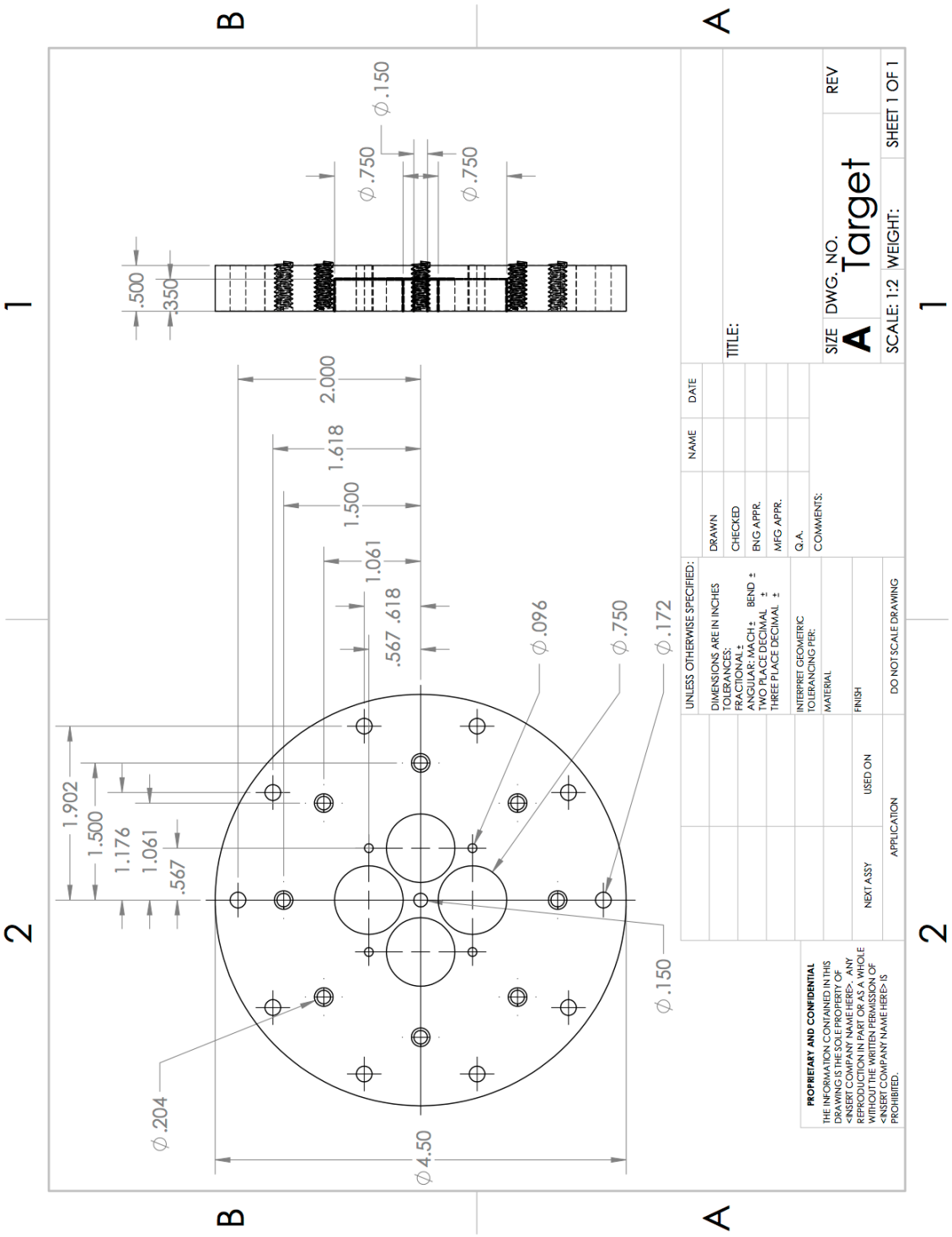

Target Back:

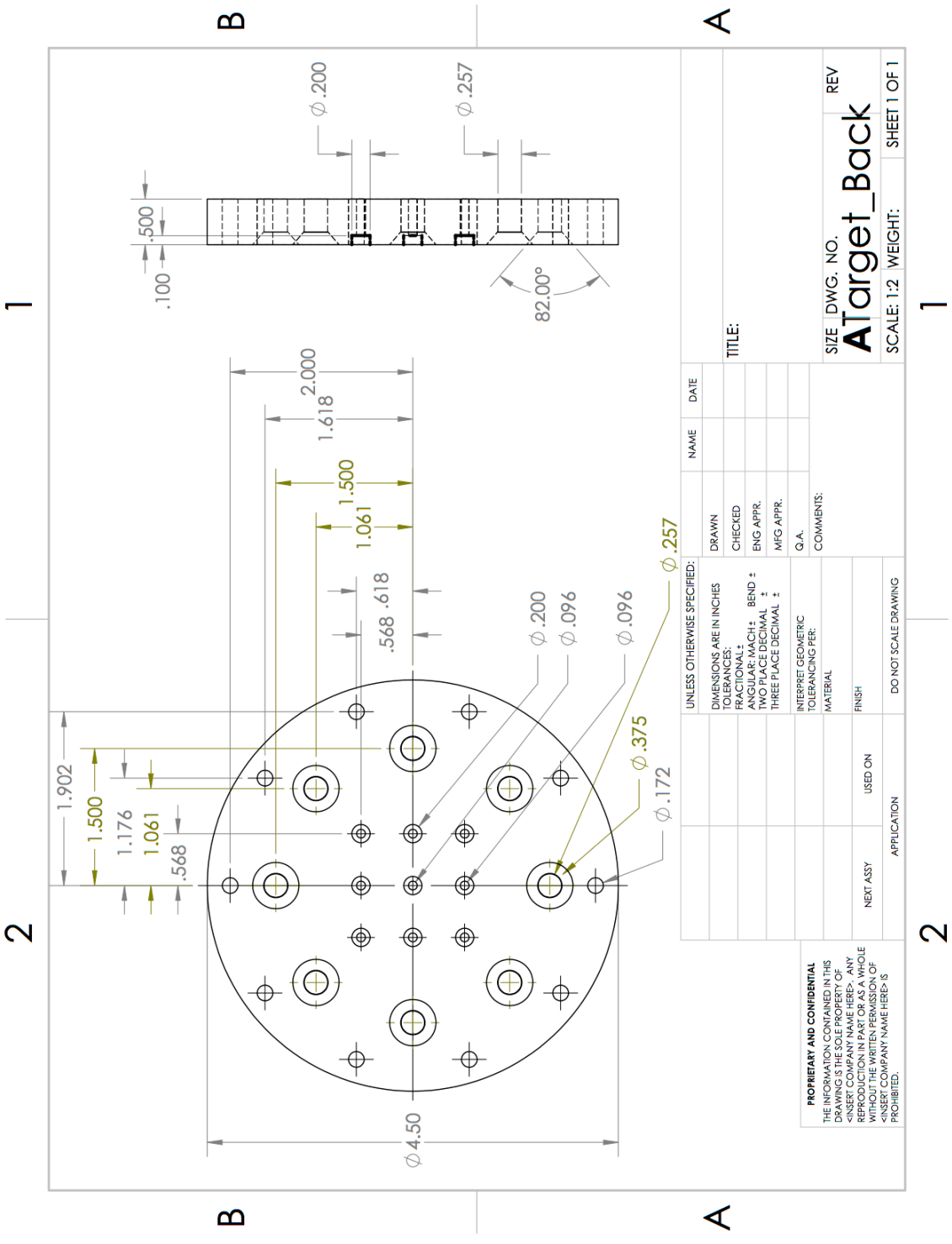
ATarget_Back
SIZE DWG. NO. REV
SCALE: 1:2 WEIGHT: SHEET 1 OF 1
TITLE:
UNLESS OTHERWISE SPECIFIED:
DIMENSIONS ARE IN INCHES
TOLERANCES:
FRACTIONAL ±
ANGULAR: MACH ± BEND ±
TWO PLACE DECIMAL ±
THREE PLACE DECIMAL ±
INTERPRET GEOMETRIC TOLERANCING PER:
MATERIAL
FINISH
DO NOT SCALE DRAWING
NAME
DATE
DRAWN
CHECKED
ENG APPR.
MFG APPR.
Q.A.
COMMENTS:
NEXT ASSY
USED ON
APPLICATION
PROPRIETARY AND CONFIDENTIAL
THE INFORMATION CONTAINED IN THIS DRAWING IS THE SOLE PROPERTY OF <INSERT COMPANY NAME HERE>. ANY REPRODUCTION IN PART OR AS A WHOLE WITHOUT THE WRITTEN PERMISSION OF <INSERT COMPANY NAME HERE> IS PROHIBITED.
Ø.200
Ø.257
.500
.100
82.00°
2.000
1.618
1.500
1.061
.568
.618
Ø.200
Ø.096
Ø.096
Ø.257
Ø.375
Ø.172
1.902
1.500
1.176
1.061
.568
Ø4.50

Momentum Trap:

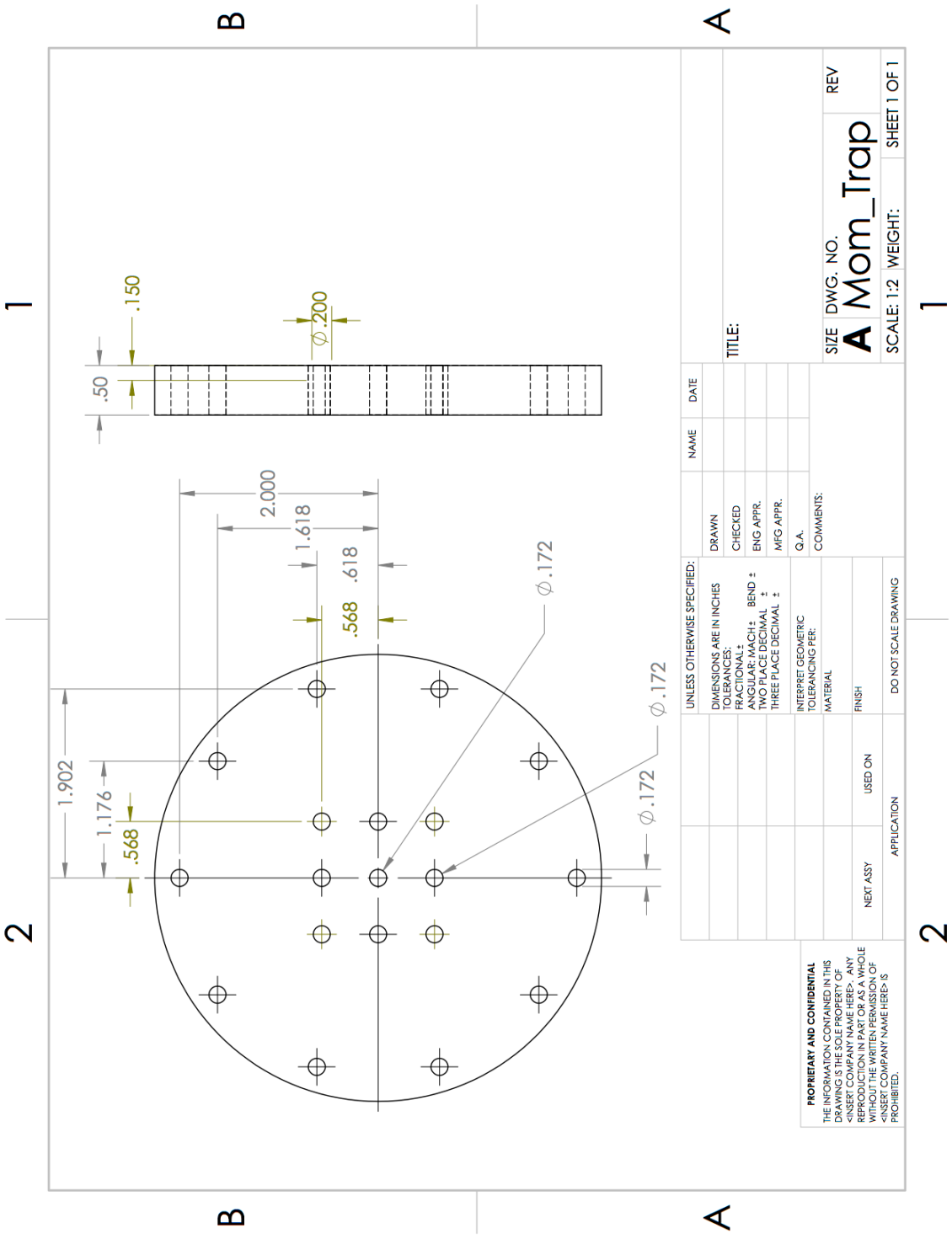

APPENDIX C – CONSOLIDATED SAMPLES

Figure 6.1: SEM images of consolidated YSZ (micro) samples from Target 10. A measured projectile velocity of 586 m/s was recorded.

YSZ (Micro) 0% wt. Graphene

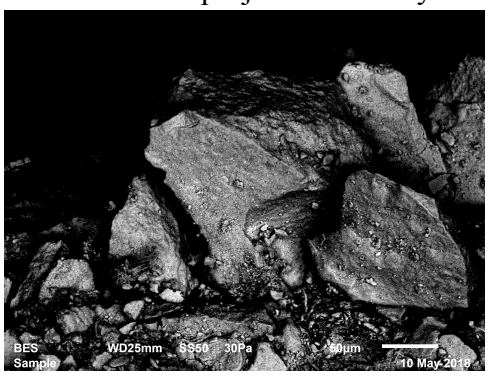

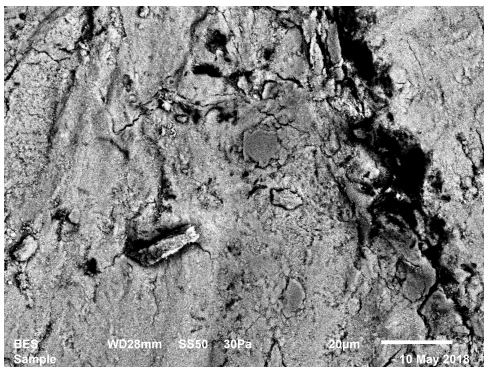

YSZ (Micro) 1% wt. Graphene

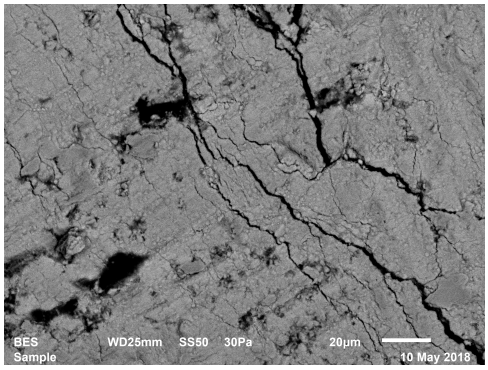

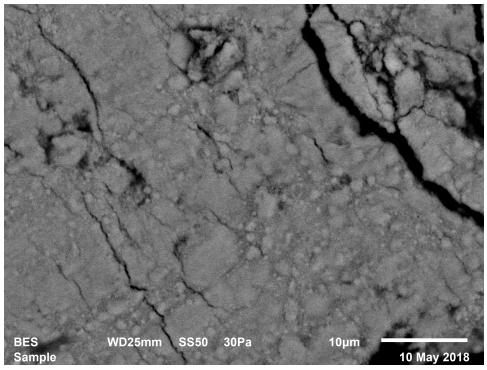

YSZ (Micro) 3% wt. Graphene

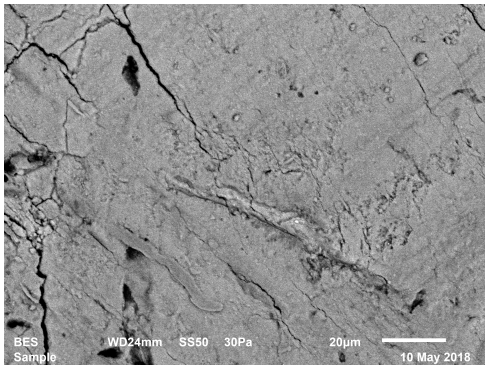

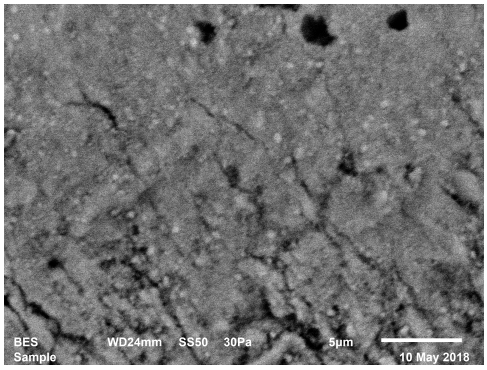

YSZ (Micro) 5% wt. Graphene